The Astrophysical Journal, 893:82 (25pp), 2020 April 10 https://doi.org/10.3847/1538-4357/ab7ffc

Massive Warm/Hot Galaxy Coronae. II. Isentropic Model

Yakov Faerman[1], Amiel Sternberg[2,3,4], and Christopher F. McKee[5]
[1] Racah Institute of Physics, The Hebrew University, Jerusalem 91904, Israel; yakov.faerman@mail.huji.ac.il
[2] School of Physics and Astronomy, Tel Aviv University, Ramat Aviv 69978, Israel
[3] Center for Computational Astrophysics, Flatiron Institute, 162 Fifth Avenue, New York, NY 10010, USA
[4] Max-Planck-Institut fur Extraterrestrische Physik (MPE), Giessenbachstr., 85748 Garching, Germany
[5] Department of Physics and Department of Astronomy, University of California at Berkeley, Berkeley, CA 94720, USA
Received 2019 September 17; revised 2020 March 9; accepted 2020 March 9; published 2020 April 17

Abstract

We construct a new analytic phenomenological model for the extended circumgalactic material (CGM) of L^* galaxies. Our model reproduces the O VII/O VIII absorption observations of the Milky Way (MW) and the O VI measurements reported by the COS-Halos and eCGM surveys. The warm/hot gas is in hydrostatic equilibrium in an MW gravitational potential, and we adopt a barotropic equation of state, resulting in a temperature variation as a function of radius. A pressure component with an adiabatic index of $\gamma = 4/3$ is included to approximate the effects of a magnetic field and cosmic rays. We introduce a metallicity gradient motivated by the enrichment of the inner CGM by the Galaxy. We then present our fiducial model for the corona, tuned to reproduce the observed O VI–O VIII column densities and with a total mass of $M_{\rm CGM} \approx 5.5 \times 10^{10}\ M_\odot$ inside $r_{\rm CGM} \approx 280$ kpc. The gas densities in the CGM are low ($n_{\rm H} = 10^{-5}$–3×10^{-4} cm^{-3}), and its collisional ionization state is modified by the metagalactic radiation field. We show that for O VI-bearing warm/hot gas with typical observed column densities $N_{\rm O\,VI} \sim 3 \times 10^{14}$ cm^{-2} at large ($\gtrsim$100 kpc) impact parameters from the central galaxies, the ratio of the cooling to dynamical times, $t_{\rm cool}/t_{\rm dyn}$, has a model-independent upper limit of $\lesssim$4. In our model, $t_{\rm cool}/t_{\rm dyn}$ at large radii is ∼2–3. We present predictions for a wide range of future observations of the warm/hot CGM, from UV/X-ray absorption and emission spectroscopy to dispersion measure and Sunyaev–Zel'dovich cosmic microwave background measurements. We provide the model outputs in machine-readable data files for easy comparison and analysis.

Unified Astronomy Thesaurus concepts: Circumgalactic medium (1879); Galaxy structure (622); Galaxy dark matter halos (1880); Quasar absorption line spectroscopy (1317); Interstellar medium (847); Galaxy formation (595); Milky Way formation (1053); Intergalactic medium (813); Galactic and extragalactic astronomy (563)

Supporting material: tar.gz file

1. Introduction

Observations of the diffuse matter around galaxies, the circumgalactic material (CGM), provide evidence for substantial reservoirs of "warm/hot" (10^5–10^6 K) gas extending to large radii from the central galaxies (Prochaska et al. 2011; Tumlinson et al. 2011a; Gupta et al. 2012; Johnson et al. 2015; Burchett et al. 2019). The warm/hot CGM is traced by absorption and emission lines of highly ionized species in the UV and X-ray (Bregman & Lloyd-Davies 2007; Henley et al. 2010; Henley & Shelton 2010). Observations also find a cool (∼10^4 K) phase in the CGM, detected through absorption features from hydrogen and lower metal ions (Werk et al. 2013; Prochaska et al. 2017). Many questions remain open, such the density and temperature distributions of the CGM and its metallicity, ionization state, and total mass (Bregman 2007; Putman et al. 2012; Tumlinson et al. 2017). Numerical simulations addressing these questions are challenging due to the high resolution required and the computational cost (Hummels et al. 2019; Peeples et al. 2019). The properties of the simulated CGM are also sensitive to the assumed physical models, such as the feedback prescriptions and physical processes on small scales (McCourt et al. 2012; Fielding et al. 2017; Ji et al. 2019; Li & Bryan 2020). Analytic models provide a different avenue to address the open questions regarding the structure of the CGM (Maller & Bullock 2004; Anderson & Bregman 2010; Miller & Bregman 2013; Mathews & Prochaska 2017; McQuinn & Werk 2018; Stern et al. 2018; Qu & Bregman 2018a; Voit 2019).

In Faerman et al. (2017, hereafter FSM17), we presented a two-phase model with separate warm and hot components for the circumgalactic corona, with the mean gas temperature constant (isothermal model) as a function of radius in each phase. We assumed that the metallicity is constant throughout the corona and found that a value of $Z' = 0.5$ solar is needed to reproduce the oxygen column densities that are measured in absorption. Large CGM gas masses, comparable to those required for "baryonic closure" of the parent galaxy halos, are also needed. Our isothermal model in FSM17 is successful in reproducing the highly ionized oxygen columns but with some challenges, such as high gas temperature and pressure in the hot phase and a short cooling time of the warm phase.[6]

In this paper, we construct an alternate model for the CGM in which we assume constant entropy (isentropic model) leading to a single phased structure with a large-scale temperature gradient from hot to warm. First, in Section 2, we present the framework of our model. We solve the equation of hydrostatic equilibrium (HSE) assuming a constant entropy adiabatic relation between the gas density and temperature, resulting in a temperature variation as a function of radius. We introduce a metallicity gradient and discuss the values for boundary conditions of the gas distributions.

[6] In this paper, we adopt the terminology used for the CGM in the literature: "warm/hot" for gas temperatures between 10^5 and 10^7 K and "cool" for ∼10^4 K gas (see also Werk et al. 2016; Prochaska et al. 2017).

In Section 3 we present our fiducial isentropic model, defined by a specific set of parameters chosen to reproduce absorption measurements of highly ionized oxygen ions (O VI–O VIII). As in FSM17, we focus on the MW and external galaxies for which O VI has been detected in the CGM. We show the gas density and temperature distributions in the model, discuss the gas ionization mechanisms, and calculate the spatial distributions of ions and gas emission properties. We then address the different timescales in the model in Section 4. We also derive a model-independent upper limit for the cooling to dynamical time ratio for O VI-bearing gas. In Section 5 we compare the model properties to observational data measured in the MW and other low-redshift L^* galaxies and provide predictions for future observations in Section 6. We compare our current model to FSM17 in Section 7, discuss the differences between our work and other models of the CGM in Section 8, and summarize in Section 9.

2. Isentropic Model

In this section, we introduce our model framework for setting the spatial distributions of the gas density, temperature, and metallicity. As in FSM17, we assume that the coronal gas is in HSE within the gravitational potential of the central Galaxy and dark matter halo, with negligible self-gravity for the gas. We assume that the gas is supported by thermal pressure, magnetic fields, cosmic rays, and turbulence. Given the evidence for turbulence in the CGM (Tumlinson et al. 2011a, 2011b; Genel et al. 2014; Werk et al. 2016), we do not imagine a perfect HSE. However, in the absence of large-scale coherent motions (inflows or outflows), there can exist a close-to-equilibrium steady state (Nelson et al. 2016; Fielding et al. 2017; Lochhaas et al. 2020). As in FSM17, we assume a spherical version of the Milky Way (MW) potential presented by Klypin et al. (2002). In Section 4 we discuss the dynamical and cooling timescales in the corona.

In FSM17, we assumed a constant (isothermal) mean temperature throughout the corona, and we invoked isobaric density and temperature fluctuations to enable simultaneous production of O VII and O VIII, and a cooling component for the O VI. Thus, FSM17 is a multiphased model, hot and at a constant mean temperature for O VII and O VIII and warm for O VI cooling out of the hot. In our new isentropic model, the altered (adiabatic) equation of state (EoS) leads to a temperature gradient, enabling production of O VI, O VII, and O VIII at differing radii but in a single phase. In our new model, we no longer require local temperature fluctuations. However, we still include turbulent motions as one of the sources of hydrostatic support. Furthermore, in our current model, we adopt a varying metallicity profile, motivated by enrichment of the CGM by the galaxy. In FSM17, we assumed constant metallicity. Finally, the gas temperature and density at the virial radius in our new model are lower than in FSM17, leading to a lower CGM pressure at the boundary with the intergalactic medium (IGM). This is more consistent with our assumption of a large-scale equilibrium and low accretion rates onto the MW halo in the recent past.

We present the HSE equation with our new EoS in Section 2.1, add a metallicity gradient in Section 2.2, and discuss the boundary conditions needed to compute the actual gas distributions in Section 2.3.

2.1. EoS and HSE

Since the Galactic corona may be heated by active galactic nucleus (AGN) feedback and star formation, we imagine that it evolves toward a convective equilibrium. We therefore adopt an adiabatic EoS relating the gas pressure and mass density,

$$P(r) = K\rho(r)^{\gamma}, \tag{1}$$

where r is the radius and K is the entropy parameter, which we assume is constant with radius. Using the ideal gas law allows us to relate the temperature to the density,

$$T(r) = K\frac{\bar{m}}{k_{\rm B}}\rho(r)^{\gamma-1}, \tag{2}$$

where $\bar{m}$ is the mean mass per particle.

For a mixture of n fluids, we can write the HSE equation as the sum of the pressures for the different components,

$$dP = \sum_{i=1}^{n} dP_i = -\rho d\varphi, \tag{3}$$

where φ is the gravitational potential. We include three pressure components, similar to those in FSM17: (i) thermal, (ii) nonthermal, from cosmic rays (CRs) and magnetic fields, and (iii) turbulent support. We assume that the density of each component is proportional to the total gravitating gas mass density ρ. For the first two components, we use the adiabatic EoS, with $\gamma_1 = 5/3$ and $\gamma_2 = 4/3$, respectively, and assume that the entropy parameter is constant with radius. For each component, $dP_i = \gamma_i K_i \rho^{\gamma_i - 1} d\rho$. For the turbulent component, we assume a constant velocity scale, $\sigma_{\rm turb}$, as we did in FSM17 and write $dP_3 = \sigma_{\rm turb}^2 d\rho$. Equation (3) is then

$$\left(\sigma_{\rm turb}^2 + \sum_{i=1,2} \gamma_i K_i \rho^{\gamma_i - 1}\right)\rho^{-1} d\rho = -d\varphi. \tag{4}$$

Integration then gives

$$\sigma_{\rm turb}^2 \ln\rho(r) + \sum_{i=1,2} \frac{\gamma_i}{\gamma_i - 1} K_i \rho(r)^{\gamma_i - 1} = D_b - \int_{r_b}^{r} \frac{GM(r)dr}{r^2}, \tag{5}$$

where r_b is a reference point, which we normally take at the outer boundary, and D_b is an integration constant.

To solve this equation for $\rho(r)$ for a given mass profile $M(r)$, we must specify $\sigma_{\rm turb}$ and K_i. The former is taken from observations of oxygen line velocities and widths (see Tumlinson et al. 2011a, the discussion in FSM17, and Section 2.3 here). For the latter—since in our model, K_i are constant with radius, they can be expressed as functions of the gas properties at the boundary r_b—the temperature, $T_{{\rm th},b}$ and density, ρ_b. For the thermal component, this is simply

$$K_1 = \frac{k_{\rm B}}{\bar{m}^{\gamma_1}} \frac{T_{{\rm th},b}}{n_b^{\gamma_1 - 1}}, \tag{6}$$

where $n_b \equiv \rho_b/\bar{m}$ is the particle volume density. To obtain K_2, we use the α parameter from FSM17, defined as $\alpha \equiv (P_{\rm th} + P_{\rm nth})/P_{\rm th} = (T_{\rm th} + T_{\rm nth})/T_{\rm th}$. For isothermal conditions, α is constant with radius. In our new model, the relative fractions of pressure support from each component vary with radius, and α is not constant. We define $\alpha_b \equiv \alpha(r_b) = (T_{{\rm th},b} + T_{{\rm nth},b})/T_{{\rm th},b}$, allowing us to write

$$K_2 = \frac{k_{\rm B}}{\bar{m}^{\gamma_2}} \frac{(\alpha_b - 1)T_{{\rm th},b}}{n_b^{\gamma_2 - 1}}. \tag{7}$$

Thus, given $\sigma_{\rm turb}$, and for the gas density, temperature, and α at the reference point, we can solve Equations (4) or (5) for the density profile, $\rho(r)$. We can then use the EoS (Equations (1)–(2)) to find the pressure and temperature profiles for each of the corona components and the total pressure profile.

2.2. Metallicity Distribution

The metal content of the CGM and its distribution are interesting for two reasons. First, the total metal content provides information on the cumulative metal production in the galaxy by star formation (Peeples et al. 2014). Second, observations of the CGM probe the gas properties, such as density and temperature, mainly through absorption and emission of radiation by metal ions (Spitzer 1956; Bregman 2007; Prochaska et al. 2009; Tumlinson et al. 2017). Thus, metals are important as tracers of the gas distribution.

In FSM17, we assumed a uniform metallicity distribution. In a more realistic scenario, the central region of the Galactic halo is expected to be enriched by metals created in supernova (SN) explosions and ejected from the disk by Galactic winds. The outer regions, close to the virial radius, may be dominated by metal-poor gas accreted from the cosmic web, resulting in a decreasing metallicity profile across the corona. Some of the accreted gas may also be pre-enriched. The level and extent of metal enrichment by outflows from the disk and the enrichment of the accreted gas depends on feedback energetics, the star formation history and distribution in the galaxy, and the physics of gas mixing and diffusion in the corona (see Fielding et al. 2018 and Li & Bryan 2020).

The main observational constraints of our model in this work are oxygen absorption measurements, probing the gas phase metallicity. The mass of metals in the CGM locked in solid-state dust grains is an additional component (Peek et al. 2015), and we do not address it here. As we discuss in Section 3, the mass of metals locked in dust is small compared to gas in our fiducial model, and we do not model the dust.

We adopt a metallicity profile given by

$$Z'(r) = Z'_0\left[1 + \left(\frac{r}{r_Z}\right)^2\right]^{-1/2}, \tag{8}$$

where Z'_0 is the Galactic metallicity and r_Z is an adjustable metallicity length scale within which the metallicity is equal to the inner metallicity Z'_0 and beyond which the metallicity decreases smoothly to the outer boundary of the CGM, which we denote by $r_{\rm CGM}$. The length scale r_Z can be set by estimating the maximal extent of outflows from the disk. Alternatively, we can set the metallicity at $r_{\rm CGM}$, and then the length scale is given by

$$r_Z = r_{\rm CGM}\left[\left(\frac{Z'(r_{\rm CGM})}{Z'_0}\right)^2 - 1\right]^{-1/2}. \tag{9}$$

The mean metallicity is given by

$$\langle Z'\rangle_V = \frac{\bar{m}}{M_{\rm CGM}}\int_{R_0}^{r_{\rm CGM}} Z'(r)n(r)dV, \tag{10}$$

where $M_{\rm CGM}$ is the CGM gas mass. The mean metallicity is calculated over the corona volume, from the inner radius, R_0, to $r_{\rm CGM}$. The total mass of metals in the corona is then

$$M_{\rm metals} = f_Z\,\langle Z'\rangle_V\, M_{\rm CGM}, \tag{11}$$

where $f_Z = 0.012$ is the mass fraction of metals at a solar metallicity, adopting the individual abundances from Asplund et al. (2009). The average line-of-sight metallicity is

$$\bar{Z}' = \frac{1}{N}\int Z'(r)n(r)ds, \tag{12}$$

where ds is the path element and N is the total gas column density along this sight line. The sight line can be calculated for an observer inside the galaxy (for MW observations) or an external observer at a given impact parameter (for other galaxies).

2.3. Boundary Conditions

In solving Equations (1)–(7), we set r_b, the reference point for the boundary conditions of the gas distribution, at the outer radius of the corona $r_{\rm CGM}$. We now discuss the value ranges we consider for $r_{\rm CGM}$ and the gas properties there, such as the density and temperature, by estimating them for the MW.

Structure formation calculations and simulations predict that matter that falls onto the galaxy is shocked and heated (White 1978; Birnboim & Dekel 2003). We define the boundary between the IGM and CGM as the location of this accretion shock. Simulations indicate that this occurs roughly, but not exactly, at the virial radius (Schaal & Springel 2015), which is estimated from the halo total mass. The mass of the MW has been measured over the last decade using a variety of methods, resulting in $M_{\rm vir} = (1.3 \pm 0.3) \times 10^{12}\ M_\odot$ (Bland-Hawthorn & Gerhard 2016). In FSM17, we used the gravitational potential profile from Klypin et al. (2002; model B; see their Table 2), which has $r_{\rm vir} = 258$ kpc, and $M_{\rm vir} = 10^{12}\ M_\odot$. These values are consistent with the range estimated by Bland-Hawthorn & Gerhard (2016), and we use the same gravitational potential and virial radius in this work.

We combine the uncertainties regarding the (i) size (and mass) of the MW halo (i.e., $r_{\rm vir}$) and (ii) location of the accretion shock into the range for $r_{\rm CGM}$ and examine values between the virial radius and $1.3\,r_{\rm vir}$, or ∼260–330 kpc. Smaller CGM radii are not implausible in theory, but they may be inconsistent with measurements of O VI in other L^* galaxies, as we discuss in Section 5.2 (see Johnson et al. 2015).

We now turn to the gas properties at this radius. First, we set the temperature, $T_{\rm th}(r_{\rm CGM})$, to the virial temperature, defined by $2E_{\rm k} = E_{\rm pot}$, where $E_{\rm pot}$ is the potential energy of the mean particle evaluated at the outer boundary. The gas temperature is then given by

$$T_{\rm vir} = \frac{G\bar{m}}{3k_{\rm B}}\frac{M(r)}{r}. \tag{13}$$

Scaling this to the Galaxy mass and $r_{\rm CGM}$, we get

$$T_{\rm vir} \approx 3.4\times10^5\ {\rm K}\left(\frac{\bar{m}}{0.59\,m_{\rm p}}\right)\left(\frac{M_{\rm vir}}{10^{12}\,M_\odot}\right)\left(\frac{r_{\rm CGM}}{300\ {\rm kpc}}\right)^{-1}, \tag{14}$$

where $0.59m_{\rm p}$ is the mean particle mass for fully ionized gas with the primordial abundance of helium. Birnboim & Dekel (2003) performed a detailed calculation of the gas temperature behind the virial shock and found a similar value. In this work, we consider

temperatures in the range $T_{\rm th}(r_{\rm CGM}) \approx (2\text{–}4) \times 10^5$ K, accounting for the uncertainty in the MW mass and the location of the shock. At these temperatures, the O VI ion fraction, $f_{\rm O\,VI}$, is close to its peak in collisional ionization equilibrium (CIE), with $f_{\rm O\,VI} \approx 0.25$ at $T_{\rm peak} \approx 3 \times 10^5$ K (Gnat & Sternberg 2007 and Section 3.2 here).

In our new model, each of the components providing pressure support behaves differently with radius due to a different EoS or adiabatic index, and the α parameter is a function of radius. For α at $r_{\rm CGM}$, we consider a range between 1 and 3, as we did in FSM17. For $\alpha = 1$, there is only thermal and turbulent support, while pressure equipartition between thermal, magnetic, and cosmic rays gives $\alpha = 3$ (see also Kempski & Quataert 2020).

For the turbulent velocity scale, we adopt $\sigma_{\rm turb} \sim 60$ km s^{-1}, similar to FSM17 (see Section 2.1 and Table 3 there). This velocity was estimated from the velocity dispersion of the O VI absorption features in the COS (Cosmic Origins Spectrograph on the Hubble Space Telecope) star-forming (SF) galaxies, reported by Tumlinson et al. (2011a). In our model, the O VI traces the extended warm/hot CGM.

To estimate the gas density at $r_{\rm CGM}$, we consider the conditions inside and outside the MW halo. McConnachie et al. (2007) inferred a lower limit of 10^{-5}–10^{-6} cm^{-3} for the Local Group (LG) intragroup medium density from ram pressure stripping of the Pegasus dwarf galaxy at $d \approx 920$ kpc from the MW. Faerman et al. (2013) used the H I distribution in Leo T to estimate an upper limit for the gas pressure in the LG. They found that at $d = 420$ kpc from the MW, $P_{\rm IGM}/k_{\rm B} \lesssim 150$ K cm^{-3}. Assuming that the pressure of the intragroup medium in the LG does not vary significantly with position on a 100 kpc scale gives an estimate for the CGM density:

$$n(r_{\rm CGM}) \sim \frac{P_{\rm IGM}}{\alpha(r_{\rm CGM}) T_{\rm th}(r_{\rm CGM}) + \sigma_{\rm turb}^2 \bar{m}/k_{\rm B}}. \quad (15)$$

For the chosen $T_{\rm th}(r_{\rm CGM})$, the adopted range of $\alpha(r_{\rm CGM})$ and $\sigma_{\rm turb}$, this gives an upper limit of $n_{\rm H}(r_{\rm CGM}) < (0.5\text{–}2) \times 10^{-4}$ cm^{-3}, where $n_{\rm H}$ is the hydrogen volume density. Another estimate is obtained at smaller distances from the Galaxy. As discussed in FSM17 (see Section 5.1 there), studies of ram pressure stripping in the Large Magellanic Cloud (LMC) and MW dwarf satellite galaxies find CGM densities of $\sim 10^{-4}$ cm^{-3} at 50–100 kpc (Grcevich & Putman 2009; Gatto et al. 2013; Salem et al. 2015), and Blitz & Robishaw (2000, hereafter BR00) found an average density of $\sim 2.4 \times 10^{-5}$ cm^{-3} inside 250 kpc. These values serve as upper limits for the density at the outer boundary, and we consider densities of $n_{\rm H}(r_{\rm CGM}) \sim (1\text{–}5) \times 10^{-5}$ cm^{-3}.

For the metallicity, we examine values in the range of $Z_0' = 0.5$–1 at the solar radius and 0.1–0.5 at $r_{\rm CGM}$. We set the upper limit at $r_{\rm CGM}$ as $Z' = 0.5$ to allow for a constant metallicity profile, for comparison with FSM17. The length scale increases from $r_Z \sim 30$ kpc for a large metallicity gradient, ranging between $Z = 0.1$ and 1, to $r_Z > 250$ kpc for flat metallicity profiles, changing by $\lesssim$25%. For a metallicity profile that varies by a factor of 3–5 between small radii and $r_{\rm CGM}$, the length scale is $r_Z \approx 50$–100 kpc. These scales are similar to the extent of galactic winds in numerical simulations (Salem et al. 2015; Fielding et al. 2017), and we prefer them in our model.

To summarize, the combination of $n_{\rm H}(r_{\rm CGM})$, $T_{\rm th}(r_{\rm CGM})$, $\alpha(r_{\rm CGM})$, and $\sigma_{\rm turb}$ allows us to compute the entropy parameters (Equations (6)–(7)), numerically solve Equation (4), and obtain the gas density profile, $\rho(r)$. Then, using the EoS, we get the individual and total pressure and temperature profiles from the outer boundary to the inner radius at the solar circle at $R_0 = 8.5$ kpc. This radius is the inner boundary in our model. In FSM17, we estimated that the thermal pressure above the Galactic disk, $P_{\rm th}(R_0)$, is between $\sim$1000 and 3000 K cm^{-3} (Wolfire et al. 2003; Dedes & Kalberla 2010). Putman et al. (2012) found pressures of $P/k_{\rm B} \sim$ 500–1300 K cm^{-3} using observations of high-velocity clouds (HVCs) at distances of 10–15 kpc from the Galactic center (GC) and 3–9 kpc above the disk. With the above observational constraints in mind, we set the boundary conditions by fixing the temperature at the outer radius ($r_{\rm CGM}$) and varying the density and nonthermal support there to set the inner pressure at R_0. Then, the metallicities at R_0 and $r_{\rm CGM}$ determine the metallicity length scale, and the distribution of metals is given by Equation (8).

3. Fiducial Model

In this section, we present our fiducial constant entropy model for a specific set of boundary conditions chosen to reproduce observations of the warm/hot CGM as traced by highly ionized oxygen absorption measured in the MW and other low-redshift galaxies (see Section 5). Table 1 summarizes the input parameters and the main properties of our fiducial model.

First, we discuss the basic gas properties, density, and temperature (Section 3.1) and the gas ionization state (Section 3.2). We show that for the gas densities in our fiducial model, photoionization by the metagalactic radiation field (MGRF) affects the metal ion fractions in addition to collisional ionization. This is in contrast with FSM17, in which the gas densities and temperatures are higher, and photoionization is negligible. We calculate the ion fractions in the CGM and the gas radiative properties using Cloudy 17.00 (Ferland et al. 2017) and the Haardt & Madau (2012) MGRF. We then present the spatial distribution of selected metal ions (Section 3.3) and the gas emission properties (Section 3.4).

3.1. Gas Distributions

Figure 1 presents the total hydrogen density and the thermal temperature profiles in the corona (left and right panels, respectively).[7] For these models, we adopt $r_{\rm CGM} = 1.1 r_{\rm vir} =$ 283 kpc. In our fiducial model, the density and temperature at this boundary are $n_{\rm H}(r_{\rm CGM}) = 1.1 \times 10^{-5}$ cm^{-3} and $T_{\rm th}(r_{\rm CGM}) = 2.4 \times 10^5$ K. Both increase inward and at R_0 are equal to 2.9×10^{-4} cm^{-3} and 2.1×10^6 K, respectively. The mean hydrogen density within $r_{\rm CGM}$ is 1.8×10^{-5} cm^{-3}.

The density, temperature, and pressure profiles are well approximated by power-law functions of the radius,

[7] We present some properties of our model as functions of the physical radius or impact parameter and others as functions of the physical scale normalized to the Galactic virial radius. The latter is done mainly when we compare the distributions in the model to the measurements in other galaxies of different sizes and masses. In each case, we present the complementary scale on the top x-axis of the plot. As in FSM17, we fit and compare our model to the SF galaxies in the COS-Halos sample. We note that this subsample has a median virial radius of 260 kpc, very similar to the value we adopt for the MW virial radius (258 kpc).

Table 1
Fiducial Model—Summary of Properties

Input Parameters	
$M_{\rm vir}$	$1.0 \times 10^{12}\ M_\odot$
$r_{\rm vir}$	258 kpc
R_0	8.5 kpc
$r_{\rm CGM}$	283 kpc ($1.1 r_{\rm vir}$)
$T(r_{\rm CGM})$	2.4×10^5 K
$n_{\rm H}(r_{\rm CGM})$	1.1×10^{-5} cm^{-3}
$\sigma_{\rm turb}$	60 km s^{-1}
α ($\alpha_{\rm OML}$)[a]	2.1 (3.2)
Z'	0.3–1.0
r_Z	90 kpc
Results	
$M_{\rm gas}(r_{\rm vir})$	$4.6 \times 10^{10}\ M_\odot$
$f_{\rm b}$ (w/o disk)[b]	0.68/0.29
$M_{\rm gas}(r_{\rm CGM})$	$5.5 \times 10^{10}\ M_\odot$
$M_{\rm metals}(r_{\rm CGM})$	$3.1 \times 10^8\ M_\odot$
$P_{\rm th}(R_0)$	1350 K cm^{-3}
$L_{\rm rad}$	9.4×10^{40} erg s^{-1}
$L_{\rm cool}$	7.6×10^{40} erg s^{-1}
$t_{\rm cool}(r_{\rm CGM})$	7.4×10^9 Gyr
$t_{\rm dyn}(r_{\rm CGM})$	3.1×10^9 Gyr
$\zeta(r_{\rm CGM})$	2.4
$\langle t_{\rm cool}\rangle$	3.6×10^9 Gyr
Approximations—$\tilde{p} \times (r/r_{\rm CGM})^{-a}$	
$\tilde{T}_{\rm th}$, $a_{\rm T}$	2.7×10^5 K, 0.62
$\tilde{n}_{\rm H}$, $a_{\rm n}$	1.3×10^{-5} cm^{-3}, 0.93
$\tilde{P}_{\rm tot}$, $a_{\rm P}$	22.1 K cm^{-3}, 1.35

Notes.
[a] Here $\alpha - 1$ gives the ratio of cosmic-ray and magnetic field pressure to thermal pressure; $\alpha_{\rm OML}$ also includes the turbulent pressure (see Section 3.1).
[b] With and without the Galactic disk mass included, assuming $M_{\rm vir} = 10^{12}\ M_\odot$ and $M_{\rm disk} = 6.0 \times 10^{10}\ M_\odot$.

$\tilde{p} \times (r/r_{\rm CGM})^{-a}$, where $\tilde{p}$ is the value of the fit at $r_{\rm CGM}$. Fits between R_0 and $r_{\rm CGM}$ give indices of $a_{\rm n} = 0.93$ and $a_{\rm T} = 0.62$ for the density and temperature, respectively. These approximations are accurate to within 20% for the density and 10% for the temperature, and they are shown in Figure 1 as dotted curves. The full approximations, including the normalization factors, are given in Table 1.

Figure 2 shows the pressure versus radius. The left panel shows the total and thermal pressures. The total pressure (black curve) at $r_{\rm CGM}$ is $P/k_{\rm B} = 20$ K cm^{-3}. This value is consistent with pressure estimates from the accretion rate onto an MW-like galaxy in cosmological simulations. The thermal pressure (red curve) at R_0 is 1350 K cm^{-3}. This is near the lower limit of the range estimated in FSM17 from observations to be between ∼1000 and 3000 K cm^{-3} (see Section 2 there). The power-law index of the (total) pressure profile is $a_{\rm P} = 1.35$, and this approximation is accurate to within 10%.

The right panel of Figure 2 shows the fractional contribution of each pressure component as a function of radius: thermal support (red), nonthermal pressure from magnetic fields and cosmic rays (blue), and turbulent pressure (green). The ratio of nonthermal to thermal pressure is parameterized by $P_{\rm nth}/P_{\rm th} = \alpha - 1$, and to include the contribution of turbulent support, we define $\alpha_{\rm OML} = P_{\rm tot}/P_{\rm th}$. With $\alpha(r_{\rm CGM}) = 2.1$ and $\alpha_{\rm OML}(r_{\rm CGM}) = 3.2$, the three components have similar contributions to the total pressure at $r_{\rm CGM}$. However, due to the higher adiabatic index of the thermal component, the thermal pressure increases more rapidly at smaller radii and dominates the total pressure at $r < 50$ kpc, with $\alpha(R_0) \sim 1.5$.

We can estimate the strength of the magnetic field implied by the nonthermal pressure. If the cosmic rays and magnetic fields have equal contributions to the energy density, the magnetic field strength in the CGM is given by $B = \sqrt{4\pi P_{\rm nth}} \propto r^{-2a_n/3}$. In our fiducial model, this results in $B \propto r^{-0.62}$, and the field increases from $B \approx 110$ nG at $r_{\rm CGM}$ to 940 nG at R_0. These values are consistent with the upper limit inferred by Prochaska et al. (2019) for the magnetic field in the CGM of a massive galaxy at $z \approx 0.36$, with $B \lesssim 500$ nG at an impact parameter of ≈30 kpc.

Given the density profile, we calculate the CGM mass and its contribution to the baryonic budget of the Galaxy. The cumulative gas mass distribution is shown in Figure 4 for spherically enclosed and projected masses (red solid and dashed curves, respectively). The coronal gas mass inside $r_{\rm vir}$ is $4.6 \times 10^{10}\ M_\odot$. Adopting a cosmological baryon fraction of $f_{\rm bar} = 0.157$ (Planck Collaboration et al. 2016), this constitutes ∼30% of the Galactic baryonic budget. Together with a mass of $\approx 6 \times 10^{10}\ M_\odot$ for the Galactic disk (McMillan 2011; Licquia & Newman 2015), we get a total baryonic mass of $\sim 1.1 \times 10^{11}\ M_\odot$, or ∼70% of the Galactic baryons expected within $r_{\rm vir}$. The total CGM mass inside $r_{\rm CGM}$ is $5.5 \times 10^{11}\ M_\odot$.

The gas phase metallicity in our model decreases from $Z' = 1.0$ at R_0 to 0.3 at $r_{\rm CGM}$ with a metallicity scale length of $r_Z = 90$ kpc and is plotted in Figure 3. The total mass of metals within $r_{\rm CGM}$ is $3.1 \times 10^8\ M_\odot$. The cumulative metal mass profiles are shown in Figure 4 for the spherically enclosed and projected masses (black solid and dashed curves, respectively). These can be useful for comparison with mass estimates from measurements of metal ion column densities (see Section 5).

For example, Peeples et al. (2014, hereafter P14) analyzed the COS-Halos O VI measurements to estimate the metal gas mass in the warm CGM. For their preferred model, with an assumed density profile slope of $a_{\rm n} = 2$, they inferred the projected metal mass inside 150 kpc and obtained $M_{\rm metals}(h < 150\ {\rm kpc}) \sim 0.46 \times 10^8\ M_\odot$, with a range of $(0.28–1.1) \times 10^8\ M_\odot$. However, P14 found that $a_{\rm n}$ has a significant effect on the total gas mass. For a profile with a slope of $a_{\rm n} = 1$, a higher-mass profile is allowed by the measurements, with $M_{\rm metals}(h < 150\ {\rm kpc}) \sim 4 \times 10^8\ M_\odot$. In our fiducial model, the projected metal mass in the gas phase within 150 kpc is $1.9 \times 10^8\ M_\odot$, within the range allowed by the different gas density distributions in P14.

Peek et al. (2015) found that galactic coronae contain significant amounts of dust and estimated a dust mass of $M_{\rm dust} \sim 6 \times 10^7\ M_\odot$ in the CGM of 0.1–1.0 L^* galaxies. This is lower than the gas phase metal mass in our model, but not negligible. Our model does not constrain the dust content of the CGM.

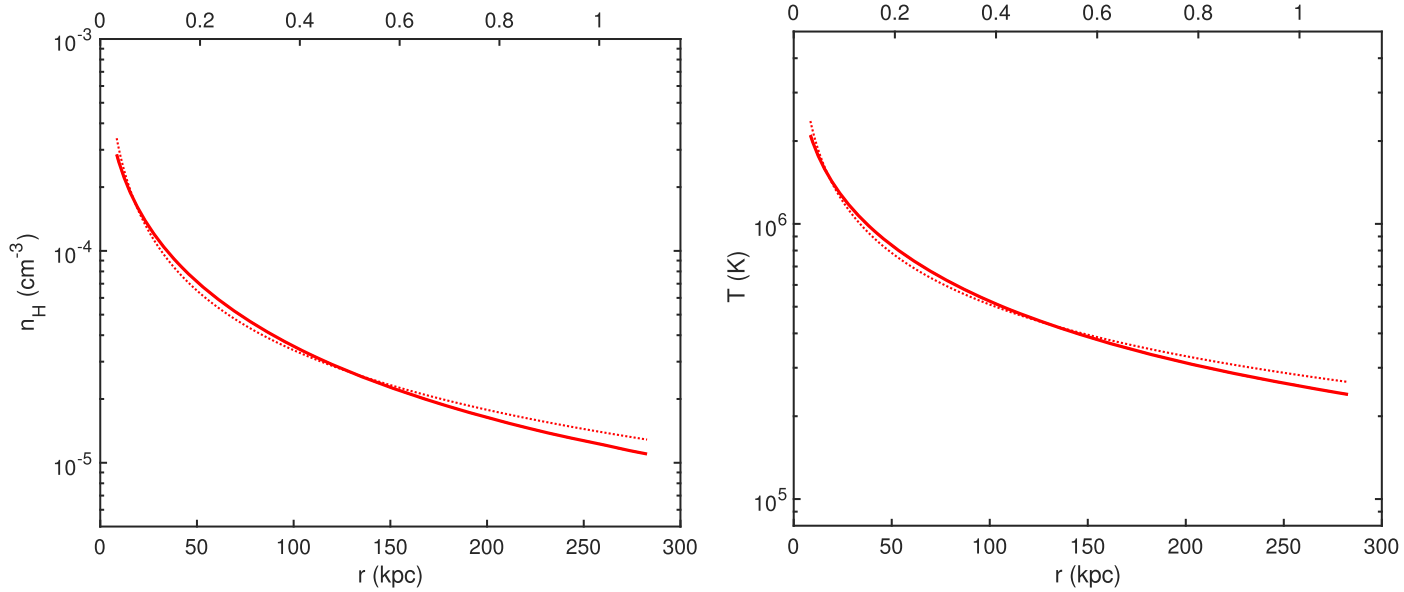

Figure 1. Gas density (left) and thermal temperature (right) profiles in our fiducial model (see Section 3.1). The solid curves show the profiles resulting from the numerical solution of the HSE equation (Equation (4)), with the boundary conditions at $r_{\rm CGM} = 283$ kpc set by the input parameters (see Table 1). The dotted curves are power-law approximations of the numerical profiles with indices of $a_{\rm n} = 0.93$ and $a_{\rm T} = 0.62$ for the density and temperature, respectively. In this work, we show the spatial coordinate in our model both in kpc (bottom axis) and normalized to the virial radius of the MW, 258 kpc (top axis).

3.2. Ionization

The warm/hot gas at each radius in our model is at a constant temperature and density given by the profiles presented in Figure 1. In computing the ionization fractions, we include electron-impact collisional ionization and photoionization by the MGRF. We assume ionization equilibrium. We do not include photoionization by stellar radiation from the Galaxy, since stellar radiation is expected to decrease rapidly as d^{-2} with the distance d from the Galaxy and is not energetic enough to affect the high oxygen ions we address here (O VI–O VIII). Other Galactic sources may have a contribution to ionizing radiation, although probably on lower ions and at small distances (see Cantalupo 2010 and Upton Sanderbeck et al. 2018). The MW and the COS-Halos galaxies do not have AGNs, and we do not include AGN radiation fields (although see Oppenheimer et al. 2018 for consideration of "fossil" O VI AGN photoionization).

In CIE, the ion fractions are functions of the gas temperature only (Gnat & Sternberg 2007). When photoionization is included, the ion fractions may also depend on the gas density and radiation field properties, such as intensity and spectral shape (Gnat 2017). For a field with a known spectral distribution, the effect of the radiation on the atomic ionization state can be estimated using the ionization parameter, given by $U \equiv \Phi/cn_{\rm H}$. Here $\Phi = 4\pi \int_{\nu_0}^{\infty} \frac{J_\nu}{h\nu} d\nu$ is the ionizing photon flux, J_ν is the radiation field energy flux density, and c is the speed of light. In our calculations, we consider the Haardt & Madau (2012, hereafter HM12) radiation field, which is a function of redshift only. For the HM12 $z = 0$ MGRF, $\Phi \approx 10^4\ {\rm cm^{-2}\ s^{-1}}$. Scaling the ionization parameter to this value and the gas density at the outer boundary of our corona model (see Table 1), we get

$$U = 3.3 \times 10^{-2} \left(\frac{\Phi}{10^4\ {\rm cm^{-2}\ s^{-1}}}\right)\left(\frac{n_{\rm H}}{10^{-5}\ {\rm cm^{-3}}}\right)^{-1}. \quad (16)$$

At $z = 0.2$, the median redshift of the COS-Halos galaxies, the ionizing photon flux of the HM12 field is $\Phi \approx 2.3 \times 10^4\ {\rm cm^{-2}\ s^{-1}}$, and we continue our calculation for $z = 0.2$.

The MGRF intensity in the EUV and soft X-rays is uncertain to some extent, with different studies arguing for a stronger (Stern et al. 2018; Faucher-Giguère 2020) or weaker (Bland-Hawthorn et al. 2017) radiation field. In this work, we adopt the HM12 spectrum and note that the FG20 and HM12 field intensities are within ∼30% of each other between 0.1 and 2 keV, the energy range relevant for the ions we address here. The differences may be larger at lower energies and are more relevant for lower ions (see Werk et al. 2016; Prochaska et al. 2017; Upton Sanderbeck et al. 2018).

The gray contours in Figure 5 show the O VI ion fraction, $f_{\rm O\ VI}$, in the temperature–density parameter space, calculated in the presence of the $z = 0.2$ HM12 MGRF using Cloudy 17.00 (Ferland et al. 2017). At hydrogen densities above $n_{\rm H} \sim 10^{-3}$ ${\rm cm^{-3}}$, the ion fraction is set by collisional ionization. It is then a function of the gas temperature only and peaks at $T_{\rm peak,O\ VI} \sim 3 \times 10^5$ K, with $f_{\rm O\ VI} \approx 0.25$. The O VI ion fraction at temperatures far from this peak, at $T < 10^5$ K ($T > 10^6$ K), is low, and oxygen exists in lower (higher) ionization states. At lower densities, below $n_{\rm H} \sim 10^{-5}$ ${\rm cm^{-3}}$, the ion fractions clearly deviate from their CIE values due to photoionization.

In general, radiation increases the overall gas ionization, but the change in the fraction of a specific ion, $f_{\rm ion}$, depends on the gas temperature compared to $T_{\rm peak,ion}$. For $T < T_{\rm peak,ion}$, energetic photons ionize the lower ionization states and increase $f_{\rm ion}$ compared to CIE. In gas at higher temperatures, radiation ionizes the atom to a higher state and reduces $f_{\rm ion}$.

We define $U_{\rm crit}$ as the threshold ionization parameter above which an ion fraction deviates by more than 10% compared to the CIE value. While the threshold can vary with temperature, for our qualitative analysis here for the O VI, we adopt a single value of $U_{\rm crit,O\ VI} \sim 7 \times 10^{-3}$. At $z = 0.2$, this corresponds to a

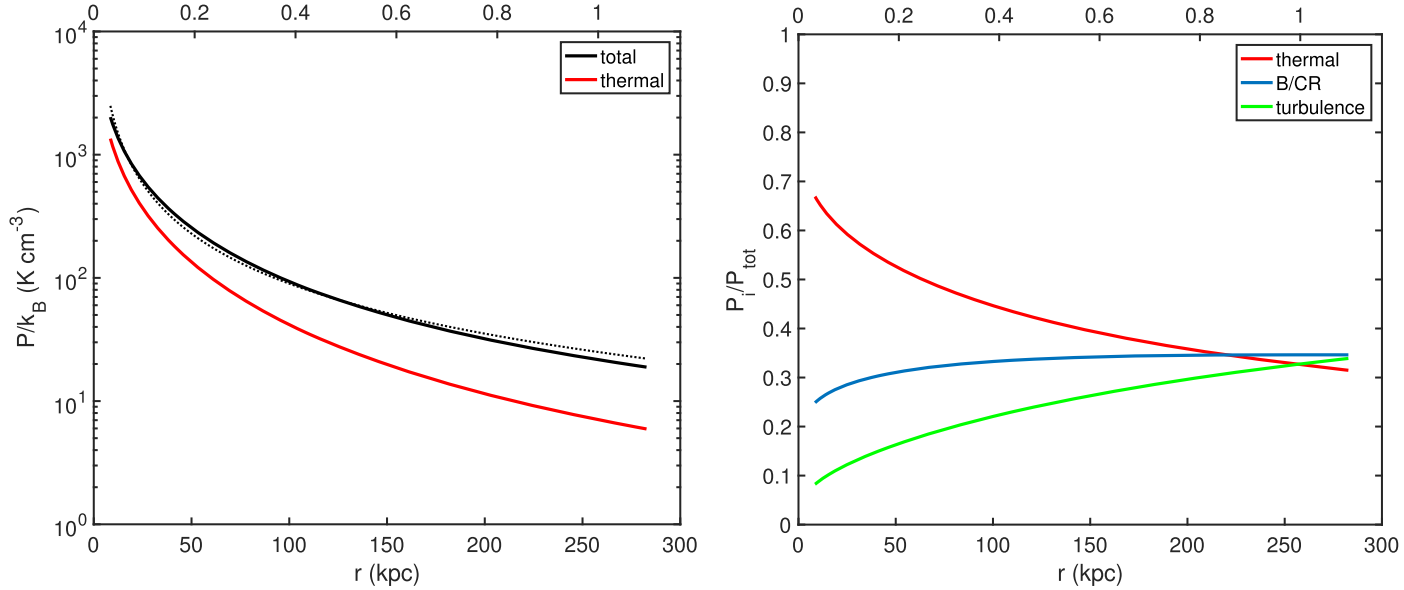

Figure 2. Pressure profiles in the fiducial corona model (see Section 3.1). Left: total (black) and thermal (red) pressure. The total pressure at the outer boundary is set by the gas temperature, density, and amount of nonthermal support ($\alpha_{\rm OML}$). The thermal pressure in the inner part is 1350 K cm^{-3}, near the lower limit of the range estimated in the MW. The total pressure profile can be approximated by a power law with an index of $a_{\rm P} \approx 1.35$, shown by the dotted curve. Right: fractional/relative pressure of the different components in the corona: thermal support (red), nonthermal pressure from cosmic rays and magnetic fields (blue), and turbulent support (green). The pressure fraction in each component varies with radius due to the different equations of state. The thermal support, with an adiabatic index of $\gamma = 5/3$, has the steepest profile. The turbulent pressure is parameterized in our model by a constant velocity dispersion (with $\sigma_{\rm turb} = 60$ km s^{-1}), and its relative fraction increases with radius.

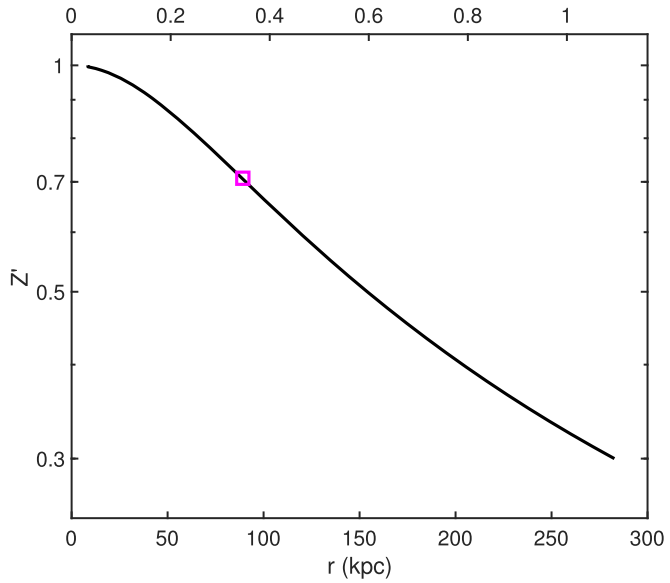

Figure 3. Metallicity profile in the warm/hot gas (see Sections 2.2 and 3.1). The magenta marker shows the metallicity length scale, $r_Z = 90$ kpc, set by the boundary conditions (Equation (9)).

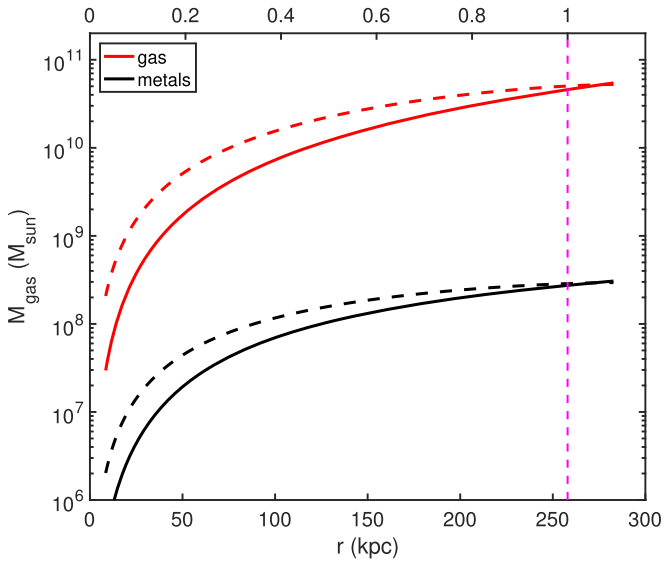

Figure 4. Cumulative gas (red) and metal (black) masses in the fiducial model. The solid curves show the spherical mass enclosed in a radius r (see Table 1), and the dashed curves show the projected mass as a function of the impact parameter. The gas mass within $r_{\rm vir}$ (marked by the vertical dashed magenta line) constitutes ≈30% of the MW baryonic budget.

density of $n_{\rm H,photo} \sim 10^{-4}$ cm^{-3}, below which photoionization is important. In Figure 5, this critical density is indicated by the vertical green dashed line.

The red line shows the $T \propto n^{2/3}$ temperature–density relation in our model (with $\gamma = 5/3$ for thermal pressure). The black squares mark specific radii between $r_{\rm CGM}$ and the solar circle. For $r \gtrsim 30$ kpc, our model has densities close to the critical photoionization density of 10^{-4} cm^{-3}. To compare the ion fraction at a given radius in the model to the fraction in CIE, one can move horizontally (at $T =$ const.) from the red curve to a density 1–2 dex above the photoionization threshold and estimate how the ion fraction changes along this line. Since most of the gas in our model is above $T_{\rm peak,O\,VI} = 3 \times 10^5$ K, photoionization reduces the O VI fraction compared to CIE. This is in contrast with models at lower temperatures, where photoionization is invoked as an O VI production mechanism (e.g., Stern et al. 2018).

The O VII and O VIII ions have photoionization densities similar to the O VI (see also Ntormousi & Sommer-Larsen 2010), and in our model, they are also affected by the MGRF. The O VI–O VIII ion fractions as functions of radius in

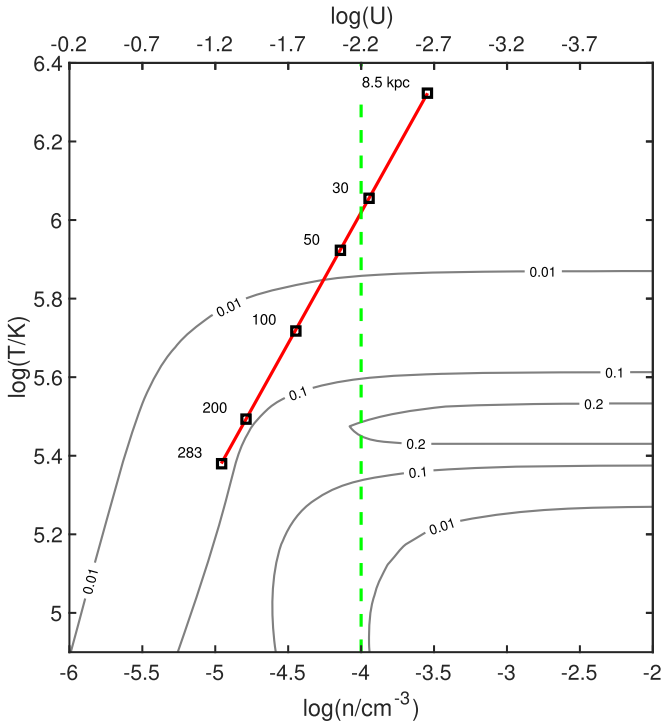

Figure 5. The O VI ion fraction (gray contours) and $T \propto n^{2/3}$ (thermal) temperature–density relation for the gas in our fiducial model (red curve). The O VI fraction is calculated in the presence of the $z = 0.2$ HM12 MGRF using Cloudy, and the gas photoionization parameter U is shown on the top x-axis. The green vertical dashed line marks the density threshold below which photoionization starts to affect the O VI ion fraction (see Section 3.2). The black squares along the red curve mark different radii in the corona in kpc. The gas density in the outer region of our model ($r \gtrsim 30$ kpc) is below the threshold density, and the temperature is above the O VI CIE peak ($\sim 3 \times 10^5$ K) out to $r \sim 200$ kpc. In this region of the parameter space, radiation reduces the O VI ion fraction, compared to its value in CIE.

our model are plotted in the left panel of Figure 6. We also display the N V fraction and discuss these curves in more detail in Section 3.3.

The total ion densities, $n_{\rm ion} = f_{\rm ion} A_{\rm i} Z' n_{\rm H}$, are also a function of the gas density and metallicity profiles and the elemental abundances $A_{\rm i}$. The volume densities of O VI–O VIII and N V are shown in the right panel of Figure 6 as a function of radius. In Section 5 we discuss the behavior of the column densities of these ions and compare them to observations.

We note that the measured O VII and O VIII column densities are associated with the MW at $z = 0$. Comparing them to the results of our model, for which we adopt the MGRF at $z = 0.2$, may seem inconsistent. However, these column densities, observed from inside the Galaxy, form mostly in the inner, denser part of the corona ($r < 30$ kpc), where their ion fractions are set by the gas temperature only (see Figure 6). Thus, using the $z = 0$ MGRF has a very small effect on the O VII and O VIII columns, and our comparison is valid (see also Section 5.1.1).

We conclude that for the gas properties of our fiducial model, photoionization by the MGRF has a nonnegligible effect on the ion fractions of the high oxygen ions (O VI–O VIII). We calculate the metal ion fractions as a function of the gas density and temperature using Cloudy 17.00 (Ferland et al. 2017) and use them to calculate the ion volume and column densities, which we discuss in Sections 3.3 and 5. The MGRF also affects the gas radiative properties through the metal ion fractions, and we calculate the gas net cooling rate and emission spectrum as a function of the density, temperature, and metallicity. In Section 3.4, we use these quantities to calculate the emission properties of the corona.

3.3. Metal Ion Distributions

Observations of the CGM reveal the gas distribution through absorption and emission by metal ions, and in this section, we describe the spatial distributions shown in Figure 6. We plot the O VI (solid blue), O VII (solid green), O VIII (solid red), and N V (solid cyan) ions. The ion fractions are shown in the left panel with the CIE fractions (dashed curves) for comparison, and the ion volume densities are shown on the right. For the nitrogen and oxygen ion densities, we use the Asplund et al. (2009) abundances, with $A_{\rm N} = 6.8 \times 10^{-5}$ and $A_{\rm O} = 4.9 \times 10^{-4}$ for solar metallicity.

The N V and O VI ion fractions are most abundant at large radii ($r \gtrsim 150$ kpc), where the gas temperature, with $T \sim 3 \times 10^5$ K, is closest to their CIE peak temperatures ($\approx$2 and 3×10^5 K, respectively). The gas density of the CGM at these radii is $\sim 3 \times 10^{-5}$ cm^{-3}, so photoionization is significant and reduces the fractions of both ions. The O VI peak ion fraction, with $f_{\rm O\,VI} \sim 0.1$, is close to its maximum at CIE ($f \approx 0.25$). The gas temperature is above $T_{\rm peak,N\,V}$, and this, together with photoionization, leads to lower ion fractions compared to O VI, with $f_{\rm N\,V} \lesssim 0.02$.

The effect of photoionization on O VII varies with radius. At intermediate radii, 30–150 kpc, the gas temperatures are such that O VII is abundant in CIE, with $f_{\rm O\,VII} \sim 1$, and photoionization reduces the O VII fraction, but the effect is small (10%–20%). At larger radii, where the temperature is below $\sim 5 \times 10^5$ K, photoionization increases the O VII fraction compared to its CIE values. The O VIII is affected more significantly. In our fiducial model, the gas temperature is high enough to form O VIII collisionally in the central part ($r \lesssim 25$ kpc). Photoionization by the MGRF creates O VIII at larger radii, and its ion fraction increases with the ionization parameter, from $f_{\rm O\,VIII} \sim 0.1$ at 30 kpc to $\sim$0.2 at $r_{\rm CGM}$. Overall, O VII is the dominant oxygen ion in our model at all radii and almost equal to the O VIII fraction at the solar circle.

The resulting densities for our four ions of interest are plotted in the right panel of Figure 6. The O VII and O VIII ion fractions do not vary strongly with radius. This leads to decreasing ion volume densities as a result of the density and metallicity distributions in the model. The N V and O VI fractions, on the other hand, increase with radius, resulting in more extended distributions with almost flat ion density profiles. The O VI volume density is in the range $n_{\rm O\,VI} \sim (2\text{–}4) \times 10^{-10}$ cm^{-3} for radii between 10 and 250 kpc. The nitrogen abundance is $\sim$7 times lower than that of oxygen, and, together with the N V lower ion fraction, this gives volume densities of $n_{\rm N\,V} \sim (4\text{–}8) \times 10^{-12}$ cm^{-3}, 20–60 times lower than those of O VI. We use the volume densities to calculate the ion column densities through the CGM, and in Section 5 we compare these to the measured values and limits.

3.4. Emission Spectrum and Cooling Rate

The left panel of Figure 7 shows the predicted emission (cooling) spectrum of the CGM in our fiducial model. The

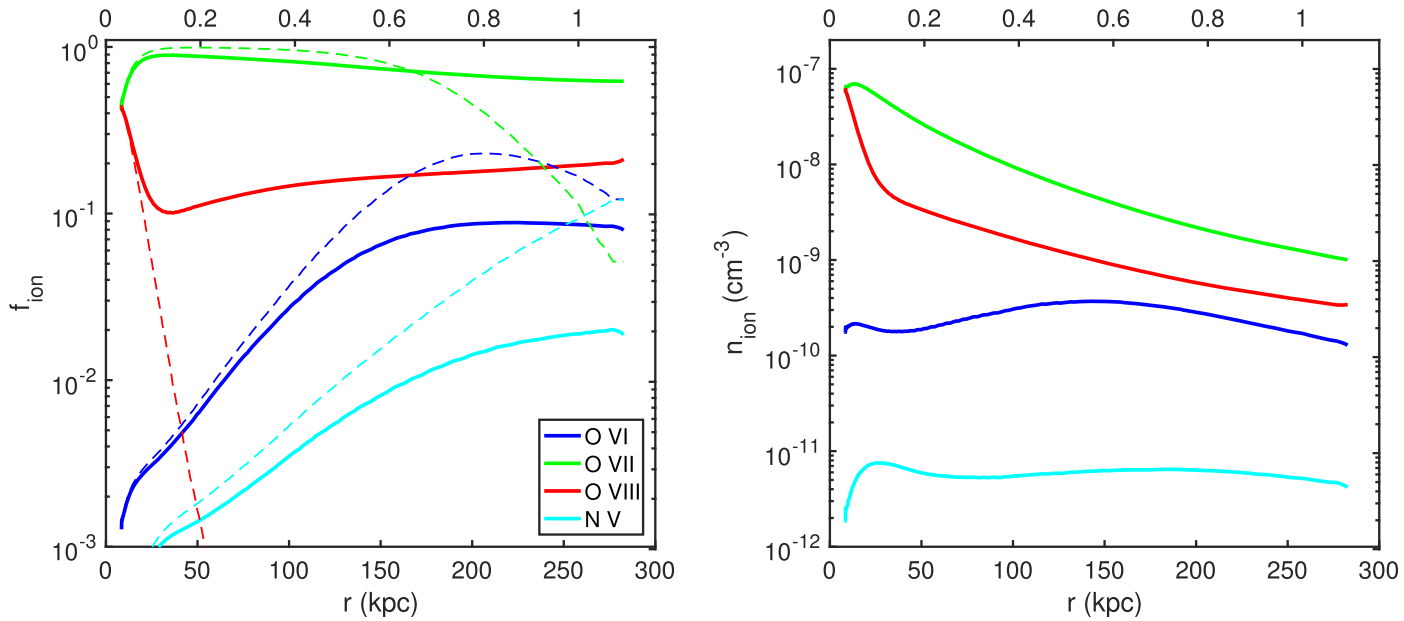

Figure 6. Distribution of selected metal ions in our CGM model: O VI (blue), O VII (green), O VIII (red), and N V (cyan). Left: ion fractions, set by collisional ionization and photoionization by the MGRF (solid curves; see Section 3.2). The dashed curves show the fractions with collisional ionization only, for comparison. The N V and O VI ions are abundant in the outer parts of the corona, where the gas temperature is low. The O VIII is created by collisional ionization in the inner part of the CGM ($r \lesssim 30$ kpc) and photoionization at larger radii. The O VII ion is dominant ($f \sim 1$) at all radii in our model. Right: ion volume densities given by the product of gas density, metallicity, elemental abundance, and ion fraction. The O VII and O VIII trace the gas density profile at $r > 30$ kpc, while the N V and O VI densities in the corona are almost constant with radius. The data used to create the right panel of this figure are available.

spectrum is given by

$$J(\nu) = 4\pi \int_{R_0}^{r_{\rm CGM}} j_\nu(n, T, Z') r^2 dr, \quad (17)$$

where j_ν is the emissivity (erg cm^{-3} Hz^{-1} sr^{-1}) of each gas parcel. We used Cloudy 17.00 (Ferland et al. 2017) to calculate the (optically thin) emissivities as functions of n, T, and Z' for gas subjected to photoionization by the $z = 0.2$ HM12 MGRF. (In FSM17, we assumed pure CIE for the emissivities.) The resulting spectrum in Figure 7 (denoted by L_ν) is displayed in units of erg s^{-1} keV^{-1} sr^{-1} and consists of collisionally excited metal ion emission lines, recombination radiation, and bremsstrahlung. The red and black lines show the full and smoothed spectra, respectively. As shown in Figure 4, the gas in our model is dominated by large radii, where the gas temperature is low, and most of the emission is in the UV. The vertical dashed lines show the 0.4–2.0 keV band.

The total luminosity[8] of the warm/hot gas is given by

$$L_{\rm rad} = \int J(\nu) d\nu \equiv 4\pi \int \mathscr{L} r^2 dr, \quad (18)$$

where $\mathscr{L}$ is the radiative cooling rate per unit volume (erg s^{-1} cm^{-3}) for each parcel. For our fiducial model, $L_{\rm rad} = 9.4 \times 10^{40}$ erg s^{-1}. The emission in the 0.4–2.0 keV band is $\sim 10^{39}$ erg s^{-1}, only $\sim$2% of the total cooling luminosity. We also compute the local net cooling rates given by $\mathscr{L} - \mathscr{H} = n_e n_{\rm H} \Lambda$, where $\mathscr{H}$ is the heating rate per unit volume[9] due to the MGRF, and Λ (erg s^{-1} cm^3) is the net cooling efficiency. In CIE ($\mathscr{H} = 0$), Λ is a function of the gas temperature and metallicity only (Gnat & Sternberg 2007). In the presence of radiation, Λ is also a function of the ionization parameter and radiation spectral shape (Gnat 2017), and we use Cloudy to calculate it. We calculate the volume-integrated net cooling rate,

$$L_{\rm cool} = 4\pi \int n_e n_{\rm H} \Lambda r^2 dr, \quad (19)$$

and find that in our fiducial model, $L_{\rm cool} = 7.6 \times 10^{40}$ erg s^{-1}. This implies that for our model, 20% of the emitted luminosity is reprocessed MGRF energy.

We integrate the spectrum in different energy bands along lines of sight through the corona to obtain the projected luminosity as a function of the impact parameter, and the result is shown in the right panel of Figure 7. The total projected emission profile (black curve) is extended, with a half-flux radius of $r_{1/2} \sim 100$ kpc. The 0.4–2.0 keV emission (solid magenta curve) comes from the hotter gas at smaller radii and is more centrally concentrated, with $r_{1/2} \sim 59$ kpc (marked by the vertical dotted line). We note that the instrumental sensitivity and background emission in the X-ray is at the level of the predicted emission. Li et al. (2018, hereafter L18) performed a stacking analysis of the X-ray emission from massive galaxies in the local universe and estimated a background level of $I \sim 10^{35}$ erg s^{-1} kpc^{-2}. This threshold is shown in our plot by a horizontal dashed magenta line. We calculate the half-flux radius of the emission above this threshold and find a value of $r_{1/2} \sim 9$ kpc, marked by the vertical dashed line in the plot. This demonstrates the challenge in detecting the CGM of MW-like galaxies in emission, given the current instrumental sensitivity and background emission. The other solid curves in the plot show the projected emission in different energy bands: $E < 13.6$ eV (blue), 13.6–400 eV (cyan), and 2–10 keV (red). As mentioned above, the total emission is dominated by the UV.

[8] The luminosity includes ionization energies released via recombinations.

[9] In our definition of $\mathscr{H}$, photoionization energy is included, in addition to the kinetic energies of the photoelectrons.

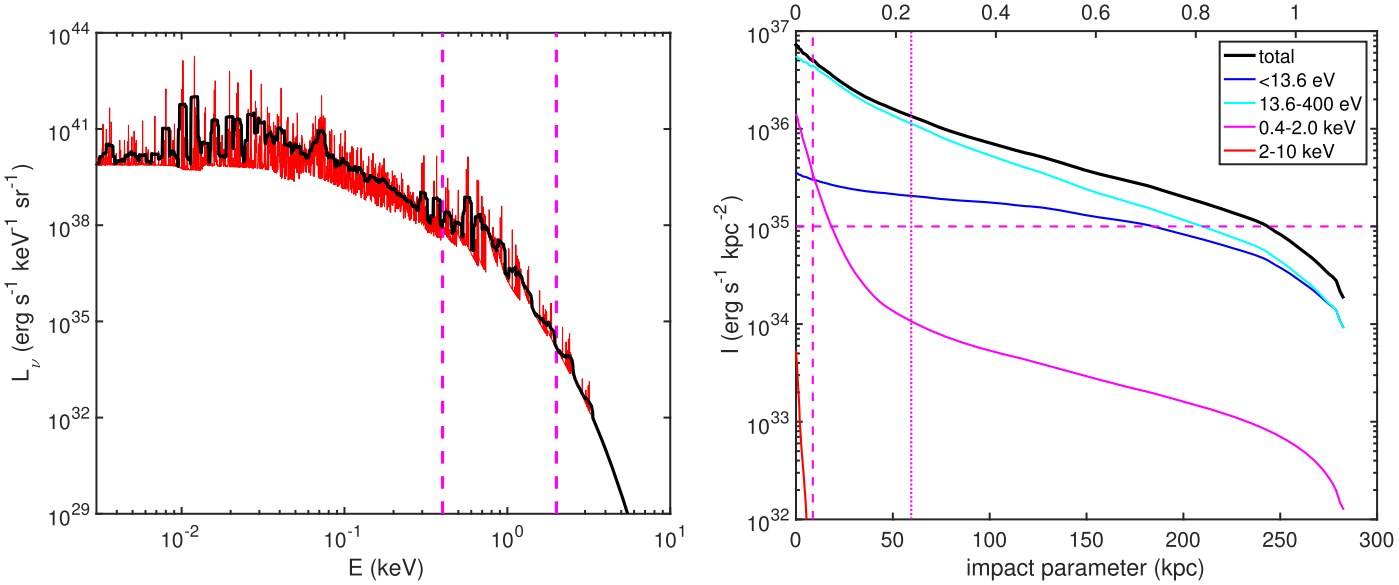

Figure 7. Emission properties of the coronal gas in our fiducial model (see Section 3.4). Left: our predicted total emission spectrum of the coronal gas (red; smoothed in black). Most of the emission is in the UV, and the luminosity in the 0.4–2 keV band (marked by magenta dashed lines) is 10^{39} erg s^{-1}, ∼2% of the total luminosity. Right: projected emission from the CGM. The emission profile of the total ionizing radiation (black curve) is extended. The soft X-ray emission in the 0.4–2.0 keV band (solid magenta curve) is more centrally concentrated, with a half-flux radius of $r_{1/2} \sim 59$ kpc (vertical dotted line). The horizontal dashed magenta line shows the detection threshold with current instrumentation, $\sim 10^{35}$ erg s^{-1} kpc^{-2}, as estimated by Li et al. (2018). The vertical dashed line shows the half-flux radius of the emission above this threshold, $r_{1/2} \sim 9$ kpc. The data used to create the right panel of this figure are available.

4. Timescales and Energetics

We now address the timescales and energy budget of the coronal gas. First, we present a model-independent upper limit for the cooling time of O VI-bearing warm/hot CGM, with the full, detailed derivation in the Appendix. We compare the cooling time, $t_{\rm cool}$, to the halo dynamical time, $t_{\rm dyn}$, and show that for an observed column density of 3×10^{14} cm^{-2} in an MW-sized halo, $t_{\rm cool}/t_{\rm dyn} \lesssim 4$ (with a range of 3–5 due to variations in the gas distribution). In our fiducial model, we show that at large radii, $t_{\rm cool}/t_{\rm dyn} \sim 2$–3. We then calculate the radiative losses and mass cooling rates in the corona and address the overall energy content of the corona. We find that there is enough energy from supermassive black hole (SMBH) and SN feedback and IGM accretion to form the CGM and sustain it over ∼10 Gyr.

For ease of comparison to previous work, we adopt the expressions used by Voit et al. (2017) for the (isochoric) cooling and dynamical times, given by

$$t_{\rm cool} = \frac{3}{2}\frac{nk_{\rm B}T}{n_{\rm e}n_{\rm H}\Lambda}, \quad t_{\rm dyn} = \sqrt{\frac{2r^3}{GM(<r)}}, \tag{20}$$

where r is the distance from the center of the galaxy/corona, and $M(<r)$ is the total mass enclosed within r.[10]

4.1. Model-independent Limit on $t_{\rm cool}/t_{\rm dyn}$

We now show that the detection of O VI in warm/hot gas implies an upper limit on the gas cooling time. We present a brief version of the analysis here and defer the full derivation to the Appendix. This result is not limited to our model and is relevant for a range of gas distributions.

To obtain an empirical upper limit, we relate the gas cooling time to the O VI column density. The latter is given by

$$N_{\rm O\,VI}(h) = 2A_{\rm O}\int_0^z n_{\rm H}(r)Z'(r)f_{\rm O\,VI}(r)dz', \tag{21}$$

where h is the impact parameter and $z' = \sqrt{r^2 - h^2}$.[11] Assuming the gas properties vary as power-law functions of the radius, we can rewrite this as

$$N_{\rm O\,VI}(h) = 2A_{\rm O}f_{\rm O\,VI}(h)n_{\rm H}(h)Z'(h)RI_a, \tag{22}$$

where R is the outer radius of the gas distribution (i.e., $r_{\rm CGM}$ in our model) and I_a is a dimensionless integral of order unity for a range of power-law slopes for $f_{\rm O\,VI}$, $n_{\rm H}$, and Z'.

The key step is to isolate the product, $n_{\rm H}Z'$, in Equation (22) and insert into the cooling time. This gives

$$t_{\rm cool}(h) = 5.8A_{\rm O}\left[\frac{k_{\rm B}T(h)f_{\rm O\,VI}(h)}{\Lambda_\odot(T,n)}\right]\frac{RI_a}{N_{\rm O\,VI}(h)}, \tag{23}$$

where we used $\Lambda = \Lambda_\odot(T,n)Z'$, ignoring cooling by hydrogen and helium and resulting in a lower limit for the cooling time. Given the shape of the cooling function and the O VI ion fraction in the temperature–density space in the presence of the HM12 MRGF at $z = 0.2$, the term in square brackets is bound from above for gas at $T > 10^5$ K, with $k_{\rm B}Tf_{\rm OVI}/\Lambda_\odot \leqslant 4.6 \times 10^{10}$ s cm^{-3}. The maximum occurs at $T \sim 3.5 \times 10^5$ K and densities above $n_{\rm H} \geqslant 10^{-4}$ cm^{-3}, where $f_{\rm O\,VI}$ is maximal (see Section 3.2). At lower densities, radiation

[10] In FSM17, we used the isobaric cooling time, longer by a factor of 5/3 and $t_{\rm dyn} = \sqrt{r^3/GM}$, shorter by $\sqrt{2}$. Thus, the ratio $t_{\rm cool}/t_{\rm dyn}$ from FSM17 should be scaled down by ≈2.35 to compare with the values adopted here.

[11] Here we assume that the warm/hot gas is volume-filling, for simplicity. In the Appendix we show that a profile for a nonunity volume-filling factor can be included in the overall functional description of the gas distribution and does not change the final result.

suppresses the cooling function, but the O VI fraction is reduced even more, so that overall, the term is smaller.[12] Finally, $I_a = 0.5 \pm 0.18$ dex for power-law slopes between 0.5 and 2.5 and impact parameters in the range $0.3 < h/R < 0.9$ (see the Appendix). Inserting these into Equation (23), we get

$$t_{\rm cool}(r = h) \lesssim 5.6 \left(\frac{R}{260\ {\rm kpc}}\right)\left(\frac{N_{\rm O\ VI}(h)}{3 \times 10^{14}\ {\rm cm^{-2}}}\right)^{-1} {\rm Gyr}, \quad (24)$$

where we scaled the corona size to the median virial radius of the COS-Halos galaxies and the O VI column density to the typical O VI column density measured at $h/r_{\rm vir} \approx 0.6$ by Tumlinson et al. (2011a; see Figure 10). The cooling time range resulting from variation in the underlying gas distributions affecting the value of I_a is ±30%.

For the halo dynamical time in Equation (20), we fit the mass distribution in the Klypin profile at large radii (where it is dominated by a Navarro–Frenk–White (NFW) profile) as $M \propto r^{0.56}$ and scale it to the MW, resulting in

$$t_{\rm dyn}(r) \approx 2.8 \left(\frac{r}{260\ {\rm kpc}}\right)^{1.22} {\rm Gyr}. \quad (25)$$

We define the ratio $\zeta \equiv t_{\rm cool}/t_{\rm dyn}$ and combine Equations (24) and (25) to give

$$\zeta(r = h) < 2.0 \left(\frac{h}{260\ {\rm kpc}}\right)^{-1.22}\left(\frac{N_{\rm O\ VI}(h)}{3 \times 10^{14}\ {\rm cm^{-2}}}\right)^{-1}. \quad (26)$$

Our approximation and the derived upper limit are valid for $0.3 < h/R < 0.9$, and the O VI column density we use is measured at $0.6\ r_{\rm vir}$. This implies $\zeta \lesssim 3.7$ (2.8–4.8 uncertainty range), much below the value of ∼10 estimated by Sharma et al. (2012a, 2012b) and Voit et al. (2017) for galaxy clusters. A ratio of $\zeta \sim 10$ would require O VI columns lower by a factor of ∼2–3 than observed in the CGM of L^* galaxies by COS-Halos.

The upper limit we derive applies to the gas responsible for the dominant part of the observed O VI absorption. For a separate, hotter component that contributes a small fraction of the total measured O VI column, the upper limit as given by Equation (23) will be higher. For example, in our FSM17 model, the O VI column forms mainly in gas that has cooled out of much hotter O VII and O VIII absorbing gas. For the cooled component, $t_{\rm cool} < 1$ Gyr, and $t_{\rm cool}/t_{\rm dyn} < 1$, consistent with our upper limit. However, for the hot component, $t_{\rm cool}/t_{\rm dyn} \sim 6$ at large radii, slightly exceeding this limit. In the isentropic model in this paper, the bulk of the CGM gas mass is traced by O VI for which the upper limit is obtained.

If gas with $\zeta < 10$ is thermally unstable and develops multiphase structure, the upper limit we derive on the O VI-bearing gas cooling time implies that cool gas should be present when O VI is detected. The COS-Halos observations seem to be consistent with this prediction, with detections of H I and low metal ions (Werk et al. 2013, 2014; Prochaska et al. 2017). In Paper III (Y. Faerman et al. 2020, in preparation), we will extend our model to include a cool ($T \sim 10^4$ K), purely photoionized gas component and compare it to existing observations.

[12] Here and throughout this work, we assumed that the coronal gas is in equilibrium. For nonequilibrium cooling, the peak O VI ion fraction is reduced by a factor of ∼2.5. The gas cooling rates for densities $\sim 10^{-4}$ cm^{-3} are similar to their equilibrium values or lower by a factor of <2. The resulting limit will be similar to its equilibrium value or even lower.

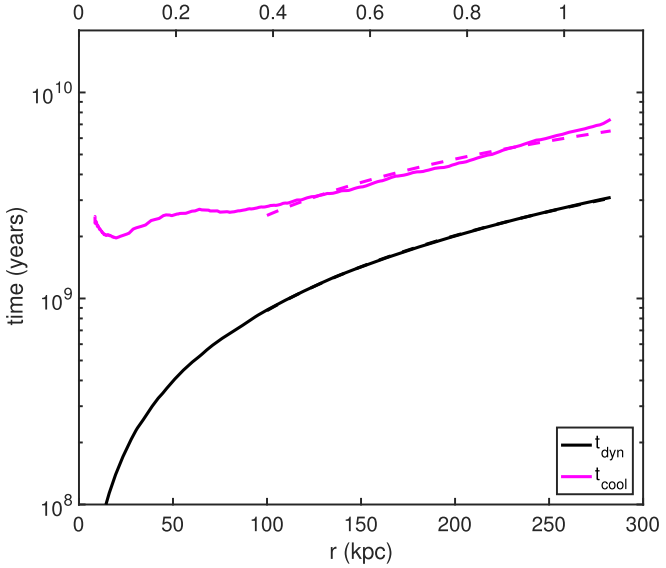

Figure 8. Dynamical time (black) and warm/hot gas cooling time (solid magenta) in our fiducial model. The decrease in gas density and metallicity leads the cooling time to increase with radius to ∼7 Gyr at $r_{\rm CGM}$. The halo dynamical time has a similar slope at large radii, and the ratio $\zeta = t_{\rm cool}/t_{\rm dyn}$ is almost constant there, with $\zeta \sim 2.5$ at $r > 100$ kpc (see Section 4.2 for details). The dashed curves show the power-law approximations to the numerical results; the dynamical time fit is hidden by the solid curve.

4.2. Model Timescales

Figure 8 shows the timescales in our fiducial model as a function of radius, calculated numerically using the definitions in Equation (20). The black curve is the dynamical time of the Galactic halo, given the Klypin et al. (2002) potential. The solid magenta curve is the gas cooling time. At large radii, $r > 100$ kpc, the two timescales are well approximated by power-law functions of the radius. The dynamical time is given by Equation (25), and the cooling time is

$$t_{\rm cool}(r) \approx 6.5 \left(\frac{r}{r_{\rm CGM}}\right)^{0.91} {\rm Gyr}. \quad (27)$$

This approximation is accurate to within 10% between 100 kpc and $r_{\rm CGM}$, and it is shown by the dotted magenta curve in Figure 8. The fit to the dynamical time is accurate to within 1% in the same range, and in the plot, the approximation is indistinguishable from the numerical calculation. Since the two timescales vary similarly with radius, their ratio is almost constant, increasing from $\zeta = 2.4$ at $r_{\rm CGM}$ to 3.1 at 100 kpc. These values are consistent with the limit derived in Section 4.1 and significantly below the value of ∼10 estimated by Voit et al. (2017) in clusters of galaxies and adopted by Voit (2019) for the CGM (see also Stern et al. 2019).

The mean global cooling timescale for the corona is the total thermal energy, $E_{\rm th} = 8.6 \times 10^{57}$ erg, divided by the net cooling rate, $L_{\rm cool} = 7.6 \times 10^{40}$ erg s^{-1}, giving $\langle t_{\rm cool}\rangle \equiv E_{\rm th}/L_{\rm cool} = 3.6$ Gyr. As discussed in Section 2, our model assumes a steady state, so that (most of) the radiative losses are offset by heating (see Section 4.3 for energy budget estimates) and the CGM is stable on an ∼10 Gyr timescale. We now briefly discuss the gas cooling properties other than $t_{\rm cool}$, which may be useful to study the energy budget of the CGM.

Figure 9 shows the distribution of local and mass cooling rates from the CGM. The left panel shows the gas radiative

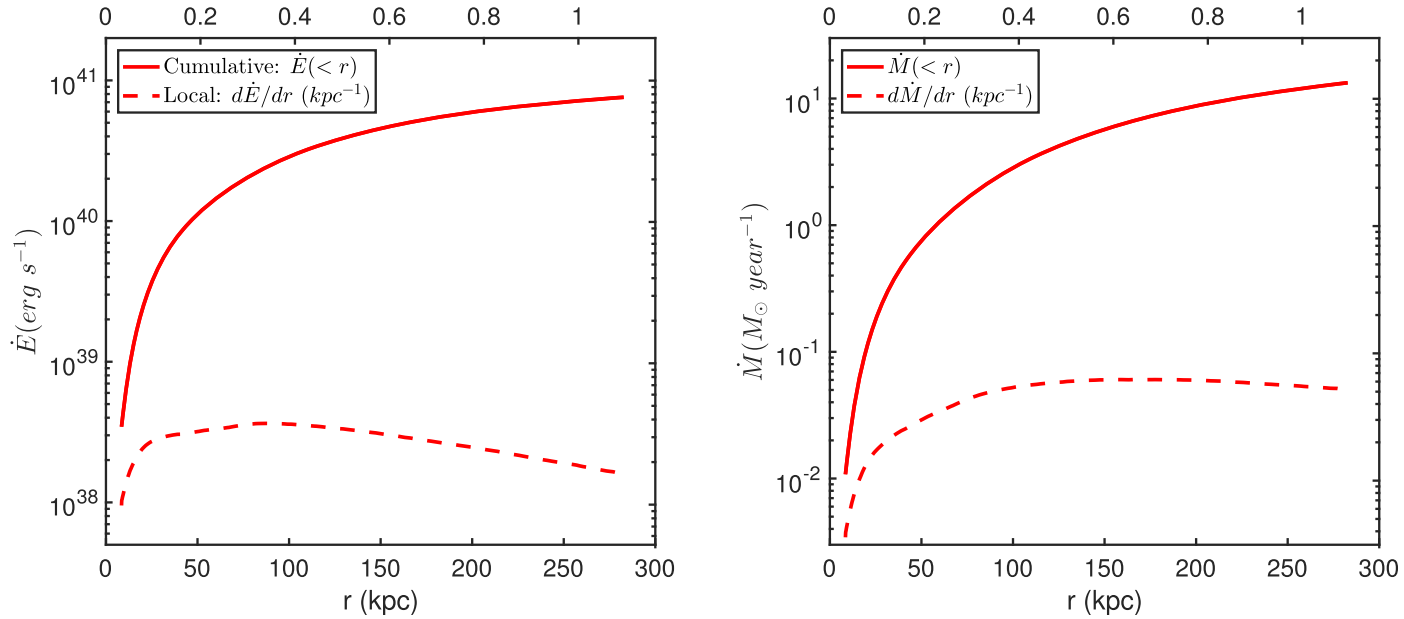

Figure 9. Radiative losses (left) and mass cooling rates (right) in the CGM. The dashed curves show the local rates in a shell per unit length (in kpc), and the solid curves are the cumulative quantities for the volume enclosed by r. The mass cooling rates are calculated as the gas mass divided by the cooling time. In our model, we assume the radiative losses are mostly offset by heating, so that the actual gas accretion rate onto the galaxy is significantly lower (see Section 4.2).

cooling rate, $\mathscr{L} = n_e n_H \Lambda$, as a function of radius. The dashed curve shows the local rate per unit length, $4\pi r^2 \mathscr{L}$, between 1.0 and 3.6 $\times$ 10^{38} erg s^{-1} kpc^{-1}. This is the distribution of energy injection rate needed to keep the CGM in a steady state and is a constraint for the mechanisms that can provide this energy. The solid curve is the integrated cumulative value inside r, with a total of 7.6 $\times$ 10^{40} erg s^{-1} inside $r_{\rm CGM}$.

Given the gas mass distribution (Figure 4) and its cooling time (Figure 8), we can calculate the gas mass cooling rate as $\dot{M}(r) = M_{\rm gas}(r)/t_{\rm cool}(r)$. Without energy input into the CGM, this gives an upper limit on the gas mass cooling out of the corona and accreting onto the galaxy (see also Joung et al. 2012; Armillotta et al. 2016; Stern et al. 2020). The right panel of Figure 9 shows the mass cooling rate, similar to the (energy) cooling rate in the left panel, with the local value per unit length as the dashed curve and the integrated value as the solid curve. The local rate is almost flat with radius, with a mass cooling rate of $d\dot{M}/dr \approx 0.05\ M_\odot\ {\rm yr}^{-1}\ {\rm kpc}^{-1}$ between 70 kpc and $r_{\rm CGM}$. The global mass cooling rate, given by $\dot{M}_{\rm tot} = M_{\rm CGM}/L_{\rm cool}$, is $\approx$13.3 $M_\odot$ yr^{-1}. Integrating this over 10 Gyr gives $\approx$1.3 $\times$ 10^{11} $M_\odot$, a factor of $\sim$2 higher than the $z = 0$ mass of the MW disk.

4.3. CGM Energetics

We now address the energy budget of the CGM in our model and the energy sources available for creating the warm/hot corona and maintaining it in a steady state.

First, we calculate the total energy in the CGM by integrating the different pressure components in our fiducial model (see Figure 2) over the volume of the corona:

$$E_{\rm CGM} = \int (E_{\rm th} + E_{\rm nth} + E_{\rm turb}) dV = \int \left(\frac{3}{2}P_{\rm th} + 3P_{\rm nth} + \frac{3}{2}\sigma_{\rm turb}^2 \bar{m} n\right) dV. \quad (28)$$

This gives a total of 2.9 $\times$ 10^{58} erg, with 29% in thermal energy, 51% in CR/B, and 20% in turbulent energy. Given the gas radiative cooling rate (see Equation (19)), we can estimate how much energy was lost from the CGM. Taking $t_{\rm life} \sim 10$ Gyr for the galaxy lifetime, we get $E_{\rm cool} = L_{\rm cool} \times t_{\rm life} \approx 2.4 \times 10^{58}$ erg. Thus, a total of $E_{\rm tot} \equiv E_{\rm CGM} + E_{\rm cool} \approx 5.3 \times 10^{58}$ erg is required to form the CGM and balance its radiative losses over the lifetime of the galaxy.

Possible energy sources for the CGM include feedback from SNe and the central SMBH and accretion onto the halo from the IGM. All three mechanisms can (i) generate shocks that heat the gas and accelerate cosmic rays and (ii) drive turbulence that amplifies magnetic fields and heats the gas when it dissipates. The SNe- and SMBH-driven outflows can advect magnetic fields and cosmic rays from the galactic disk to the CGM. We use MW data to estimate the energy budget available to fuel the CGM.

We estimate the total energy injected into the CGM by SNe over the lifetime of the galaxy as

$$E_{\rm SNe} \approx M_{*,\rm MW} \times R_{\rm SN} \times E_{\rm SN,s} \times f_{\rm SN}, \quad (29)$$

where the terms on the right-hand side are the MW present-day stellar mass, the mean number of SNe per unit of stellar mass, the total energy for a single SN event, and the fraction of that energy that goes to the CGM. We take $M_{*,\rm MW} = 5 \times 10^{10}\ M_\odot$, $R_{\rm SN}$ of one SN event per 100 $M_\odot$, and $E_{\rm SN,s} = 10^{51}$ erg. The coupling factor, $f_{\rm SN}$, is uncertain, and for $f_{\rm CGM} = 0.1$, we get $E_{\rm SNe} \approx 5.0 \times 10^{58}$ erg. Next, we estimate the energy from SMBH feedback. The mass of the MW SMBH, Sgr A*, is $M_{\rm MW,SMBH} = 4.1 \times 10^6\ M_\odot$ (Gravity Collaboration et al. 2019). Assuming $f_{\rm SMBH} = 0.03$ of the rest mass was converted to kinetic energy by the accretion disk (Sadowski & Gaspari 2017), we get $E_{\rm SMBH} \approx 2.2 \times 10^{59}$ erg.

We estimate the contribution of gas accretion from the IGM onto the galactic halo to the energy budget. We do this

Table 2
Fiducial Model—Comparison to Observations

	FSM17 (Isothermal)	Isentropic Model (This Paper)	Observations	References
$\sigma_{\rm oxygen}$ (km s^{-1})	72	60	67.2 (54.5–79.7)	(a), (b)
$P_{\rm th}(R_0)$ (K cm^{-3})	2200	1350	1000–3000	(c), (d)
DM (LMC) (cm^{-3} pc)	17.4	8.8	$\lesssim$23	(e), (f)
$n_{\rm H}$(50–100 kpc) (cm^{-3})	(0.83–1.3) $\times$ 10^{-4}	(0.35–0.72) $\times$ 10^{-4}	$\sim$10^{-4}	(g), (h)
$\langle n_{\rm H}\rangle_{250\ {\rm kpc}}$ (cm^{-3})	4.6 $\times$ 10^{-4}	2.0 $\times$ 10^{-5}	$\sim$2.5 $\times$ 10^{-5}	(i)
MW Absorption (Section 5.1.1)				
$N_{\rm O\ VII}$ (cm^{-2})	1.6 $\times$ 10^{16}	1.2 $\times$ 10^{16} (L_s = 33.2 kpc)	1.4 (1.0–2.0) $\times$ 10^{16}	(j), (k), (o)
$N_{\rm O\ VIII}$ (cm^{-2})	3.8 $\times$ 10^{15}	3.4 $\times$ 10^{15} (L_s = 11.6 kpc)	3.6 (2.2–5.7) $\times$ 10^{15}	(l), (o)
O VII/O VIII ratio	4.5	3.6	4.0 (2.8–5.6)	(b), (k), (l)
MW Emission (Section 5.1.2)				
$S_{0.4-2.0}$ (erg s^{-1} cm^{-2} deg^{-2})	0.82 $\times$ 10^{-12}	0.33 $\times$ 10^{-12}	2.1 (1.9–2.4) $\times$ 10^{-12}	(m)
$I_{22\ \text{Å}}$ (L.U.)[a]	1.2	0.57(L_s = 5.2 kpc)	2.8 (2.3–3.4)	(n)
$I_{19\ \text{Å}}$ (L.U.)[a]	0.33	0.17(L_s = 3.2 kpc)	0.69 (0.58–0.83)	(n)
22 Å/19 Å ratio	3.6	3.3	4.3 (3.4–5.5)	(b), (n)

Notes.
[a] L.U.= photons s^{-1} cm^{-2} sr^{-1}.
References. (a) Tumlinson et al. (2011a), (b) FSM17, (c) Wolfire et al. (2003), (d) Dedes & Kalberla (2010), (e) Anderson & Bregman (2010), (f) Prochaska & Zheng (2019), (g) Grcevich & Putman (2009), (h) Salem et al. (2015), (i) Blitz & Robishaw (2000), (j) Bregman & Lloyd-Davies (2007), (k) Fang et al. (2015), (l) Gupta et al. (2012), (m) Henley et al. (2010), (n) Henley & Shelton (2010), (o) Das et al. (2019).

by calculating the gravitational energy in the CGM, $E_{\rm acc} = f_{\rm acc} \times (GM_{\rm halo}/r_{\rm CGM}) \times M_{\rm CGM}$, where $f_{\rm acc}$ is a numerical coefficient of order unity accounting for the growth of the Galaxy with cosmic time. For our fiducial model, this results in $E_{\rm acc}/f_{\rm acc} \approx 1.7 \times 10^{58}$ erg. While it is subdominant compared to the energy outputs of SNe and the SMBH, accretion provides an energy source at the outer boundary of the halo that is different from SN and SMBH feedback, which injects energy at the base of the corona.

The energy from SNe and SMBHs is injected from within the galaxy. The observations show that the CGM at large radii (>100 kpc) is metal-enriched (Tumlinson et al. 2011a; Prochaska et al. 2017), providing evidence for extended galactic outflows. Numerical simulations also suggest that winds driven by SN and SMBH feedback can transport energy and metals to large radii in the halo (McNamara & Nulsen 2007; Bower et al. 2017; Fielding et al. 2017; Li & Tonnesen 2019). However, we do not consider specific transport processes in this paper.

For the gas densities in our model, the equilibrium temperatures for heating by the MGRF are $\sim 2 \times 10^4$ K, significantly lower than the gas temperatures in the model. As noted in Section 3.4, only 20% of the total computed luminosity (shown in Figure 7) is reprocessed MGRF energy.

To summarize, our estimate shows that there is enough energy available in an MW-like galaxy to form and power the CGM. We have shown that SNe and energy injection by Sgr A* can offset the radiative losses over $\sim$10 Gyr. The energy from SN events is sufficient to power the CGM for a coupling constant of $f_{\rm SN} = 0.1$. The energy from SMBH feedback is a factor of $\sim$4 higher than that from SNe, and if a significant fraction of this energy was injected into the CGM, it could have ejected gas beyond the virial radius.

One important feature of the COS-Halos O VI measurements (Tumlinson et al. 2011a) is the bimodality in the presence of O VI absorption, with detections around SF galaxies and only upper limits in passive galaxies with sSFR $\lesssim 4 \times 10^{-12}$ yr^{-1}. Our model framework does not directly relate the O VI column to the star formation rate (SFR) in the galaxy, but it is consistent with several possible explanations for such a relation. One option is that since the O VI-bearing gas at $T \sim 3 \times 10^5$ K has a high cooling efficiency, it requires energy input to prevent it from cooling, as discussed above. In our model, we assume that the radiative losses of the CGM are balanced, and we have shown that SNe, as driven by star formation, can indeed offset these losses. Another scenario, explored by Oppenheimer et al. (2016) using the EAGLE simulations, is that both the SFR and the O VI are independently correlated to the halo (and stellar) mass. In this case, the halo mass with the peak SFR happens to be the same as the halo mass at which the CGM temperature corresponds to the O VI CIE peak. Similarly, in our model, the gas temperature at the outer boundary is related to the halo mass and size (see Equation (13)). In either scenario, (a) halos hosting galaxies with low star formation or (b) higher-mass halos may have hotter coronae with lower cooling efficiencies and longer cooling times. These coronae may be detectable through UV and X-ray absorption of higher metal ions.

5. Comparison to Observations

In FSM17, we presented a summary of observational data, mainly UV/X-ray emission and absorption, probing warm/hot gas around the MW and other L^* galaxies in the nearby universe (see Section 2 and Table 1 there). We start by addressing these data, first those of the MW (Section 5.1) and then those of other galaxies (Section 5.2). For the latter, we consider additional observations, including measurements of O VI absorption around and beyond the virial radius (Johnson et al. 2015) and N V absorption (Werk et al. 2013, 2016).

Table 2 summarizes the values of the quantities we discuss, comparing our fiducial isentropic model to observations and our FSM17 isothermal model.

5.1. Milky Way

Blitz & Robishaw (2000) estimated the CGM density needed to explain the observed dearth of gas in MW dwarf satellite galaxies and found a mean value of $\langle n_{\rm H}\rangle \approx 2.5\times10^{-5}$ cm^{-3} inside 250 kpc. Grcevich & Putman (2009) performed a similar analysis for satellites at distances of 50–100 kpc and found densities around 10^{-4} cm^{-3}. Salem et al. (2015) used simulations to reproduce the distribution of ram pressure–stripped gas around the LMC (at a distance of 50 kpc) and estimated a coronal gas density of $1.10^{+0.44}_{-0.45}\times10^{-4}$ cm^{-3}. In our fiducial model, the mean density of warm/hot gas inside 250 kpc is $\langle n_{\rm H}\rangle_{250\,\rm kpc}\approx 2.0\times10^{-5}$ cm^{-3}. The gas densities at 50–100 kpc in our model are in the range $\sim$(0.4–0.7) $\times10^{-4}$ cm^{-3}, a factor of $\sim$2 lower than the values estimated by Grcevich & Putman (2009) and Salem et al. (2015). They are also lower by a factor of $\sim$2 than the densities in our FSM17 isothermal model. We note that estimates from ram pressure–stripped systems may be biased toward the denser regions of the corona.

Manchester et al. (2006) presented dispersion measure (DM) measurements to pulsars in the LMC. Anderson & Bregman (2010) discussed these and estimated an upper limit of DM $\leqslant$ 23 cm^{-3} pc for the CGM component. Prochaska & Zheng (2019) used the same observations and estimated DM $=23\pm10$ cm^{-3} pc. In our model, the computed DM in the corona to the LMC is DM $=8.8$ cm^{-3} pc, consistent with the Anderson & Bregman (2010) upper limit.

5.1.1. O VII and O VIII Absorption

The O VII and O VIII column densities for our model are $N_{\rm O\,VII}=1.2\times10^{16}$ and $N_{\rm O\,VIII}=3.4\times10^{15}$ cm^{-2}. These are consistent with the observed values of 1.4 (1.0–2.0) $\times10^{16}$ and 3.6 (2.2–5.7) $\times10^{15}$ cm^{-2}, respectively (1σ error ranges). The ratio of the column densities in our model is $N_{\rm O\,VII}/N_{\rm O\,VIII}=3.6$, close to the value of 4.0 (2.8–5.6) we estimated in FSM17 from observations.

To quantify where most of the column is formed, we define the scale length, L_s, as the distance along the line of sight from the solar circle to the point where the column density is half of its total value at $r_{\rm CGM}$. For our fiducial model, the O VII and O VIII scale lengths are $\approx$33 and 12 kpc, respectively. The length scales are smaller than in our FSM17 isothermal model ($\sim$50 kpc for both ions) for two reasons. First, the metallicity in our new model decreases outward, compared to the constant metallicity we assumed in FSM17. Second, the temperature gradient leads to a different distribution for each ion (see Figure 6). The O VII is abundant for a wide range of temperatures and therefore extends to larger radii, resulting in $L_s\sim30$ kpc. On the other hand, O VIII forms mostly in the inner hot part of the corona and has a more compact distribution. Since radiation affects the ion fractions mostly at large radii ($r>L_s$; see Section 3.3), adopting the $z=0.2$ rather than the $z=0$ radiation field does not make a significant difference here. We verify this by by recalculating the fiducial model using the $z=0$ MGRF and find that the O VII/O VIII columns for an observer inside the galaxy change by less than 3%.

Das et al. (2019, hereafter D19a) detected $z\approx0$ absorption from the highly ionized species N VII, Ne IX, and Ne X along a single sight line toward the blazar 1ES1553. They attributed these absorptions to an additional hot, $\sim10^7$ K, CIE component within the CGM of the Galaxy. However, they commented that it is uncertain how ubiquitous such hot gas might be (see also Pezzulli et al. 2017). Our model does not include gas at such high temperatures.

5.1.2. X-Ray Emission: O VII/O VIII Lines and 0.4–2.0 keV Band

For an observer at R_0, the X-ray emission along a line of sight in our model is centrally concentrated with length scales of $\sim$3–5 kpc. These are smaller than the emission length scales in FSM17, mainly since the higher-temperature gas in the inner part of the corona is more emissive in the X-ray compared to the cooler gas at larger radii. The decreasing metallicity profile also contributes to the decrease in the gas emissivity, since metal ions constitute a significant fraction of the total emission at $\sim$1 keV.

The 22 and 19 Å feature emission intensities in our fiducial model are $I_{22\,\text{Å}}=0.58$ and $I_{19\,\text{Å}}=0.18$ L.U. (line units: photons s^{-1} cm^{-2} sr^{-1}). These account for $\sim$20%–25% of the observed values, with $I_{22\,\text{Å}}=2.8$ (2.3–3.4) and $I_{19\,\text{Å}}=0.69$ (0.58–0.83) L.U. (1σ errors). The line intensities ratio, $I_{22\,\text{Å}}/I_{19\,\text{Å}}=3.3$, is also below the observed value of 4.3 (3.4–5.5). The X-ray emission intensity in the 0.4–2.0 keV band in our model is 3.3×10^{-13} erg s^{-1} cm^{-2} deg^{-2}. This constitutes 16% of the emission intensity measured by Henley et al. (2010), with 2.1 (1.9–2.4) $\times10^{-12}$ erg s^{-1} cm^{-2} deg^{-2} (see Table 1 in FSM17).

Since the emission is centrally concentrated, its intensity depends strongly on the density (or pressure, for similar temperatures) near the solar circle. To test the conditions needed to reproduce the observed emission, we construct a higher-pressure model, with $P(R_0)/k_{\rm B}\sim3000$ K cm^{-3}, that still reproduces the O VI–O VIII observations (by keeping the gas density–metallicity product constant). In this model, the emission intensities are $I_{22\,\text{Å}}\approx1.6$ and $I_{19\,\text{Å}}\approx0.5$ L.U., and the band emission is $S_{0.4-2.0}=1.0\times10^{-12}$ erg s^{-1} cm^{-2} deg^{-2}. This is higher by a factor of $\sim$3 compared to our fiducial model and closer to, but still below, the MW values. However, reproducing the measured values requires $P(R_0)/k_{\rm B}\sim4500$ K cm^{-3}, significantly higher than suggested by observations of HVCs above the MW disk and a factor of $>$3 higher than in our fiducial model, with $P/k_{\rm B}=1350$ K cm^{-3}.[13] Furthermore, such a model exceeds the DM upper limit estimated to the LMC, with DM ≈30 cm^{-3} pc. As we discussed in FSM17, an alternative explanation is that most of the X-ray emission originates in the hot interstellar medium in the Galactic disk, not included in our model.

5.2. External Galaxies

5.2.1. O VI and N V Absorption

For the O VI absorption data, we combine two sets of observations. The first are measurements from the COS-Halos survey described in FSM17,[14] probing impact parameters of

[13] Our isothermal model in FSM17 was normalized to a thermal pressure of $P/k_{\rm B}=2200$ K cm^{-3} at R_0.

[14] We note that the COS-Halos SF galaxies have a relatively narrow halo mass range—90% of the galaxies with O VI detections have masses between 3×10^{11} and 2×10^{12} $M_\odot$ (see Figure 3 in McQuinn & Werk 2018). Thus, modeling the COS-Halos SF galaxies using the MW halo is a reasonable approximation. The virial temperature scales as $M_{\rm vir}^{2/3}$, giving a factor of $(20/3)^{2/3}\approx3.5$, or ±0.27 dex. This is similar to the scatter in the O VI column density measurements in the CGM of these galaxies (see Figure 10 here).

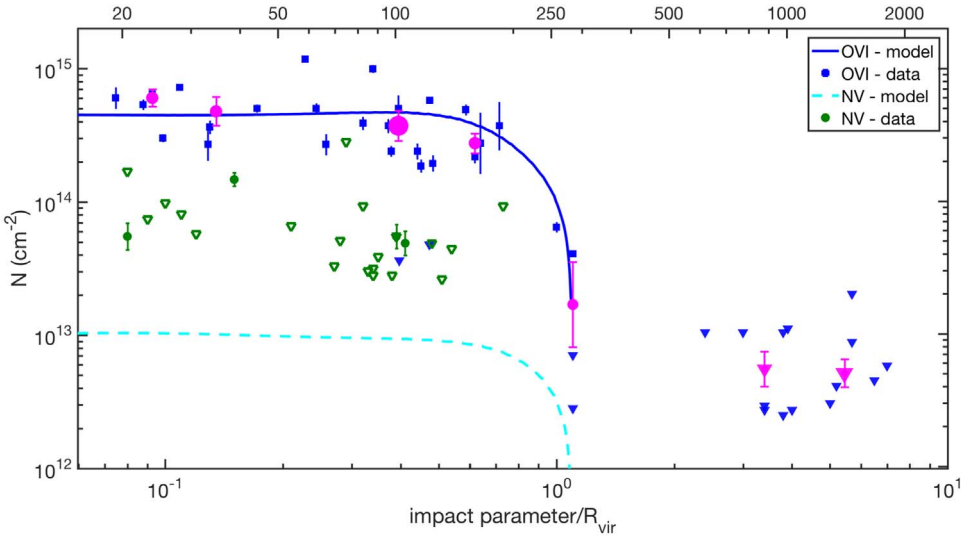

Figure 10. The O VI and N V column density profile observations and model. The data are shown as a function of the impact parameter normalized by the virial radius on the bottom axis, and the physical impact parameter for our model is given on top. The blue symbols are the O VI column density measurements (squares) and upper limits (filled triangles), taken from the COS-Halos (Tumlinson et al. 2011a) and eCGM surveys (Johnson et al. 2015). The magenta circles show the O VI binned data, with the symbol size and error bars indicating the number of objects and the scatter in the bin. The green symbols are the N V data taken from COS-Halos (Werk et al. 2013), with filled circles and open triangles for the measurements and upper limits, respectively. The solid blue and dashed cyan lines show the O VI and N V column density profiles in our fiducial model (see Section 5.2). The O VI absorption is detected out to $h \sim r_{\rm vir}$, with only upper limits at larger impact parameters. The value of $r_{\rm CGM} = 1.1 r_{\rm vir}$ in our models is chosen to reproduce this distribution. Our model predicts that the N V column densities in the CGM of MW-like galaxies are a factor of ∼3–10 below the current upper limits.

$h \lesssim 0.6\ r_{\rm vir}$. The second set consists of measurements from the eCGM survey, presented by Johnson et al. (2015) and extending out to 5–10 virial radii of the observed galaxies. Beyond $r_{\rm vir}$, Johnson et al. (2015) reported mostly upper limits for the O VI column densities, typically below 10^{13} cm^{-2} (see Figure 3 there). Since we aim to model MW-like galaxies, we select from this sample the isolated SF galaxies with stellar masses above $\sim 3 \times 10^9\ M_\odot$, similar to the SF galaxies in the COS-Halos sample. This results in 18 measurements, and the combined data set (COS-Halos and eCGM) is shown in Figure 10 by blue symbols, with measured columns as squares and upper limits as filled triangles.

The O VI data can be well approximated by a simple step function. Within approximately the virial radius ($h \lesssim r_{\rm vir}$), the profile is consistent with a constant column density of $\sim 4 \times 10^{14}$ cm^{-2}. At $h \sim r_{\rm vir}$, the column density drops sharply, with only nondetections at larger impact parameters. For $3\ r_{\rm vir} < h < 7\ r_{\rm vir}$, the median upper limit is $\sim 7 \times 10^{12}$ cm^{-2}, a factor of ∼50 lower than the typical column density measured by COS-Halos. For a clearer comparison to our model, we bin the individual measurements in radius in logarithmic intervals, taking the median column density in each bin and estimating the error as the scatter. The binned data are shown by the magenta markers, with the marker size proportional to the number of objects in the bin. The O VI column density profile for our model is the blue solid curve in Figure 10, consistent with the binned data points at $h/r_{\rm vir} > 0.1$. The CGM distribution in our model ends at $r_{\rm CGM} = 1.1 r_{\rm vir}$, chosen to be consistent with the few O VI detections at $h \sim 1.1 r_{\rm vir}$ and the nondetections at larger impact parameters.

In the COS-Halos sample, Werk et al. (2014) searched for N V absorption and reported upper limits for most sight lines. For the SF galaxies in the sample, 20 out of 24 sight lines have upper limits for the N V column densities. The COS-Halos N V data are shown in Figure 10 by green symbols, with the nondetections as open triangles and measured columns as filled circles. The median upper limit on the N V column density is 5×10^{13} cm^{-2}, with a scatter of <0.3 dex. The cyan dashed curve shows the N V column density profile in our fiducial model. The profile is almost constant with impact parameter, with $N_{\rm N\,V} \approx 10^{13}$ cm^{-2}, consistent with the measured upper limits. Thus, our model predicts that the N V column densities in the CGM of MW-like galaxies at low redshift are a factor of ∼3–10 below the current upper limits.

The four sight lines with detected N V absorption have column densities between ∼0.5 and $\sim 1.5 \times 10^{14}$ cm^{-2}. Three of the galaxies associated with these sight lines have stellar masses below $1.5 \times 10^{10}\ M_\odot$. This is a factor of 3–4 lower than the MW stellar mass and below the median stellar mass of the COS-Halos SF subsample, $M_* \approx 2 \times 10^{10}\ M_\odot$. In CIE, the N V ion fraction peaks at $\sim 2 \times 10^5$ K. These galaxies may have lower halo masses and virial temperatures closer to this value than our fiducial model, leading to an increase in the N V column. The sight line associated with the fourth galaxy has an impact parameter of $h/r_{\rm vir} \sim 0.15$, and the detected absorption may also be contaminated by gas associated with the galactic disk.

5.2.2. X-Ray Emission

The emission properties of our model are shown in Figure 7, with the computed emission spectrum presented in the left panel and the projected intensity profile for an external observer in the right panel.

Observationally, only a handful of galaxies have been detected in X-ray emission so far, all in the local universe and more massive than the MW. Some detections of X-ray emission around massive spirals have been attributed to high star formation in the disk (Strickland et al. 2004; Tüllmann et al. 2006). More recently, Das et al. (2019) combined X-ray imaging and spectral analysis and reported the detection of

extended emission around NGC 3221, a massive spiral galaxy with SFR $\sim 10\ M_\odot\ \mathrm{yr}^{-1}$, out to impact parameters of $\sim$150 kpc. Focusing on galaxies with SFRs similar to the MW, Pedersen et al. (2006) used Chandra to measure X-ray emission around NGC 5746 and reported a 0.3–2.0 keV luminosity of $L_X \sim 4.4 \times 10^{39}$ erg s^{-1}. Rasmussen et al. (2009) reanalyzed these observations with updated calibration data and added observations of NGC 5170. They did not detect significant emission in either galaxy and placed a 3σ upper limit of 4.0×10^{39} erg s^{-1} on the X-ray luminosity. The projected integrated bolometric luminosity in our model inside 40 kpc is 1.5×10^{40} erg s^{-1}. The emission in the 0.4–2.0 keV band is 4.4×10^{38} erg s^{-1}, consistent with the limit by Rasmussen et al. (2009).

The X-ray emission intensity profiles of several massive galaxies ($M^* > 1.5 \times 10^{11}\ M_\odot$) were measured by L18, observed as part of the CGM–MASS survey. They used stacking analysis and detected emission in the 0.5–1.25 keV band at the level of $\sim 10^{35}$–10^{36} erg s^{-1} kpc^{-2} out to $\sim$150 kpc from the galaxies, or $h \sim 0.3$–$0.4\ r_{\rm vir}$. They found that the projected intensity profile decreases as a power-law function of the impact parameter, scaling as $I \propto h^{-a}$, with $a = 1.4$–1.5, in the range of $h/r_{\rm vir} \sim 0.03$–0.6. The emission in this band in our model has similar intensities in the inner part but a slightly steeper profile, with a power-law slope of $a = 1.7$.

We note two important differences between the MW CGM and that of more massive galaxies. First, the halo virial temperature scales with the halo mass and radius as $T_{\rm vir} \propto M_{\rm vir} r_{\rm vir}^{-1} \propto M_{\rm vir}^{2/3}$ (see Equation (13)). Higher gas temperatures can produce the overall stronger emission reported by Pedersen et al. (2006). Second, for median cosmological halos, the halo concentration, $C \equiv r_{\rm vir}/r_s$ (where r_s is the halo scale radius; see Sternberg et al. 2002), decreases with halo mass (Dutton & Macciò 2014). For a given halo mass, lower concentrations result in more extended dark matter distributions and flatter gravitational potentials. The combination of lower concentrations and higher gas temperatures may lead to flatter gas density distributions and emission profiles compared to the MW, consistent with the results by L18. Additional parameters in our model may vary with galaxy mass, such as the ratio of thermal to nonthermal support, the turbulent velocity scale in the CGM, etc. An exploration of the variation in halo mass and its effect on the properties of the CGM is beyond the scope of this paper.

6. Predictions for Future Observations

In this section, we present the observational predictions of our model. We calculate the column densities of different metal ions that are present in the warm/hot gas and can be observed in UV and X-ray absorption. We use the calculated spectrum of the corona to predict the emission intensity profiles in different energy bands. We predict the DM for observations of pulsars and/or fast radio bursts (FRBs), and we calculate the radially dependent Compton y-parameter for comparison to the Sunyaev–Zel'dovich (SZ) distortions inferred from cosmic microwave background (CMB) measurements. We show these quantities for observations of the MW and other galaxies. The results presented here are available online for comparison to other models and observational data.

6.1. Milky Way

The O VII and O VIII absorption at $z \sim 0$ has been measured in the X-ray-brightest QSOs with $\sim$30–40 O VII detections and a handful of sight lines with O VIII (Bregman & Lloyd-Davies 2007; Gupta et al. 2012; Miller & Bregman 2013). Fang et al. (2015) searched for a correlation of the O VII column density with Galactic latitude or longitude and found that existing data are consistent with a constant column density profile. However, current absorption observations in the X-ray often have significant uncertainties due to limited sensitivity and spectral resolution. Future X-ray observatories will provide measurements for a larger number of sight lines with higher accuracy (Kaastra et al. 2013; Smith et al. 2016; The Lynx Team 2018), and we calculate the O VII/O VIII column distributions in our model to be tested by these observations.

We plot the predicted O VII and O VIII column densities in the left panel of Figure 11. Since our model is spherically symmetric, for an observer inside the Galaxy, the column densities, as well as other quantities, are a function only of the angle, $\theta_{\rm GC}$, from the GC. As described in Sections 3.3 and 5.1.1, the O VII ion is abundant at all radii in the CGM, and its half-column length scale, $L_s \sim 30$ kpc, is relatively large compared to R_0. Thus, for an observer at $r \sim 10$ kpc, the O VII column density (green curve) is almost constant with $\theta_{\rm GC}$, consistent with current observations (Fang et al. 2015). The O VIII ion, on the other hand, is formed mostly in the central part of the CGM, and its length scale is smaller ($\sim$10 kpc). Thus, the column density at small $\theta_{\rm GC}$, with 6×10^{15} cm^{-2}, is higher by a factor of $\sim$2–3 than at large angles from the center (red curve).

The DM can provide a strong constraint on the total gas column, since it is independent of the gas metallicity. Today, the DM has been measured for pulsars in the LMC/SMC at a distance of $\sim$50 kpc (Crawford et al. 2001; Manchester et al. 2006; Ridley et al. 2013). Upcoming facilities (e.g., LOFAR and SKA; van Leeuwen & Stappers 2010; Keane et al. 2015) with higher sensitivities may be able to find pulsars in other, more distant satellites of the MW and measure their DMs. In the left panel of Figure 12, we show the DM in our model as a function of the angle from the GC for distances of $d = 50$, 150, and 250 kpc from the GC (solid black, blue, and red curves, respectively). The magenta circle marks the LMC at $\theta_{\rm GC} = 81°$ with 8.8 cm^{-3} pc. Future DM measurements for extragalactic sources (FRBs, for example) may provide constraints on the total DM of the MW CGM. In our model, the contribution from $r > 250$ kpc is small, and integration out to $r_{\rm CGM}$ gives values of DM $\sim$13–21 cm^{-2} pc (dashed black curve), close to the values at 250 kpc.

Prochaska & Zheng (2019) estimated the DM of the MW CGM at $\sim$50–80 cm^{-3} pc, integrating to the virial radius. However, this results from models with a large CGM mass,[15] and hence gas density. Their CGM mass is a factor of $\sim$3 higher than in our model, and scaling down their values for the DM by the same factor gives 17–27 cm^{-3} pc. This is similar to the range in our model when integrated to $r_{\rm vir}$, as shown by the solid red curve in Figure 12. This demonstrates the usefulness of (accurate) DM measurements to constrain the gas density and total mass in the CGM.

[15] The density profiles in Prochaska & Zheng (2019) are scaled to give a total CGM mass of $0.75\Omega_b/\Omega_m M_{\rm halo} \sim 1.8 \times 10^{11}$ for $M_{\rm halo} = 1.5 \times 10^{12}\ M_\odot$, estimated for the MW.

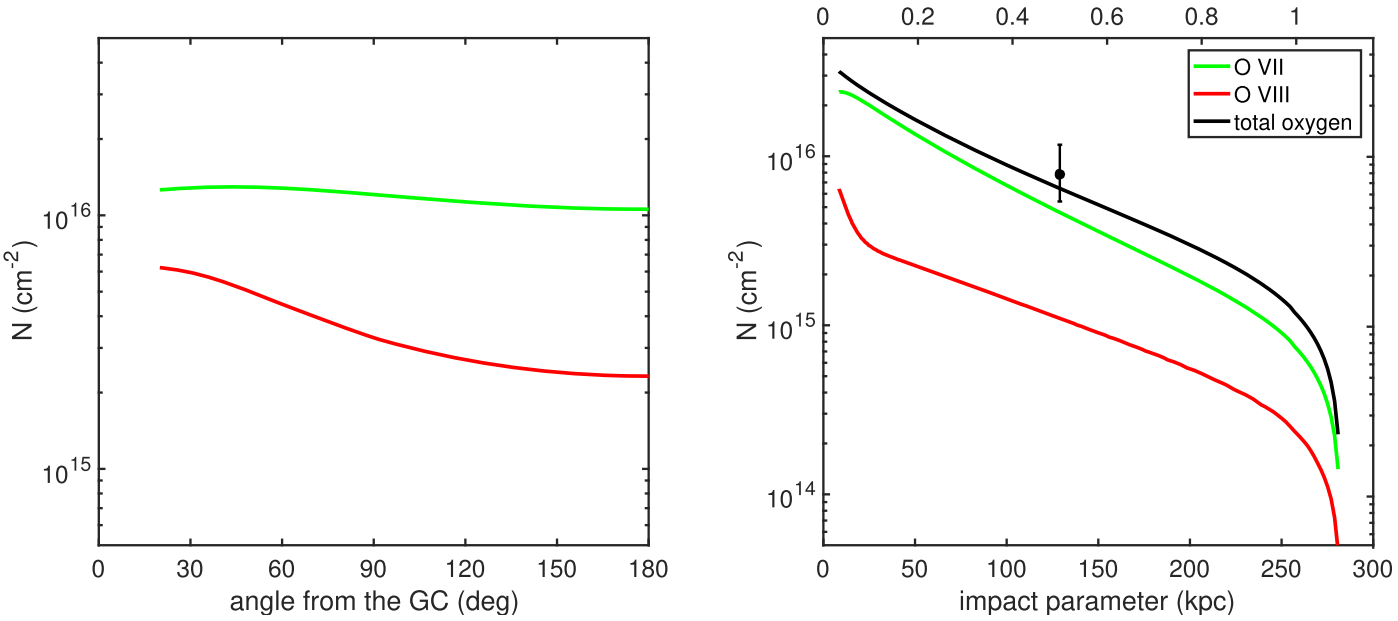

Figure 11. The O VII (green) and O VIII (red) column densities in our fiducial model. Left: columns as a function of the angle from the GC for an observer inside the galaxy at $R_0 = 8.5$ kpc. The volume O VII distribution is extended, with a length scale of ∼30 kpc, and the column density does not vary strongly with θ_{GC}. The O VIII is formed mainly in the inner, high-temperature part of the CGM, and the column density away from the GC is lower (see Section 6.1). Right: columns for an external observer, looking through the CGM at an impact parameter h. The O VII and O VIII columns at ∼10 kpc are a factor of 2 higher than the observed values for the MW. The marker shows the total oxygen column measured by Nicastro et al. (2018) in the WHIM, with a nearby galaxy at a projected distance of $h = 129$ kpc. The total oxygen column in our model (black curve) at this impact parameter is consistent with the measurements, suggesting that a significant fraction of the detected absorption may originate in the CGM rather than the IGM (see Section 6.2.1). The data used to create the right panel of this figure are available.

6.2. External Galaxies

6.2.1. UV and X-Ray Absorption

For the MW, UV and X-ray absorption from hot gas has been detected. However, in the X-ray, absorption observations at $z \sim 0$ lack kinematics due to the limited spectral resolution of current instrumentation. In the UV, the detected absorption lines are spectrally resolved, and their kinematics are measured. Nevertheless, the exact location of the absorbing gas is still unclear due to the complex dynamics of the disk–CGM interface (Zheng et al. 2015, 2019; Martin et al. 2019).

Measurements of O VII and O VIII absorption in other galaxies (similar to the COS-Halos O VI observations) will better determine the extent of the hot CGM and be more sensitive to low surface density gas compared to emission observations. In the UV, ions such as N V, O VI, Ne VIII, and Mg X probe different gas temperatures and can be helpful in constraining the CGM properties. We use our model to predict the column densities for such future observations (Kaastra et al. 2013; The LUVOIR Team 2018). We present the column density profiles for an external observer both as a function of the physical impact parameter and normalized to r_{vir}.

The right panel of Figure 11 shows the column density profiles of O VII and O VIII versus impact parameter h in our fiducial model (green and red curves, respectively). As discussed above, the O VII ion fraction is high and almost constant across the wide range of temperatures in our model, and the resulting O VII column density profile is extended. It is well fit by an exponential profile, $\log(N_{O\,VII}) \propto (-h/L_N)$, with a scale of $L_N \sim 0.63\, r_{vir}$ set by the metallicity gradient and the gas density profile. The O VIII column (red), on the other hand, has a two-part profile. In the inner regions ($h < 25$ kpc), the O VIII ion fraction is controlled by collisional ionization and decreases rapidly with temperature. This gives a column density profile that has a strong dependence on the impact parameter, with $N \sim 7 \times 10^{15}$ cm^{-2} at 10 kpc. In the outer part, the O VIII fraction is set by photoionization and increases with radius between 30 kpc and r_{CGM} (see Figure 6). The resulting column density profile in the outer part is well fit by an exponential function with $L_N \approx r_{vir}$, flatter than the O VII.

Nicastro et al. (2018, hereafter N18) reported the discovery of O VII absorption in the warm/hot intergalactic material (WHIM). They presented measurements of total oxygen column densities for two absorbers with $7.8^{+3.9}_{-2.4} \times 10^{15}$ and $4.4^{+2.4}_{-2.0} \times 10^{15}$ cm^{-2} at $z = 0.434$ and 0.355, respectively. They searched for possible associations of these absorbers with galaxies, and for the first system, they found a spiral galaxy at a similar redshift and a projected distance of 129 kpc (although see Johnson et al. 2019, suggesting that this absorption is associated with the blazar environment). Assuming this galaxy is indeed associated with the absorber and is similar to the MW, we can compare the measured column to our model. The total oxygen column density from N18 is shown by the black circle in the right panel of Figure 11 (including the 1σ errors reported by the authors). The black curve shows the total oxygen column density in our fiducial model. At an impact parameter of $h = 129$ kpc, our model predicts $N_O = 3.0 \times 10^{15}$ cm^{-2}, dominated by the O VII ion, with $N_{O\,VII} = 2.3 \times 10^{15}$ cm^{-2}. This suggests that a nonnegligible fraction of the observed absorption could originate in the warm/hot CGM of the galaxy adjacent to the line of sight, rather than the IGM. Information regarding the stellar or total mass of this galaxy will allow for scaling the impact parameter to the virial radius and performing a better comparison to our model. Furthermore, separating the CGM contribution from the total column will allow a better estimate of the IGM properties. The closest galaxy to the second absorber found by N18 is at a projected distance of 633 kpc, and a similar association with the CGM is less likely.

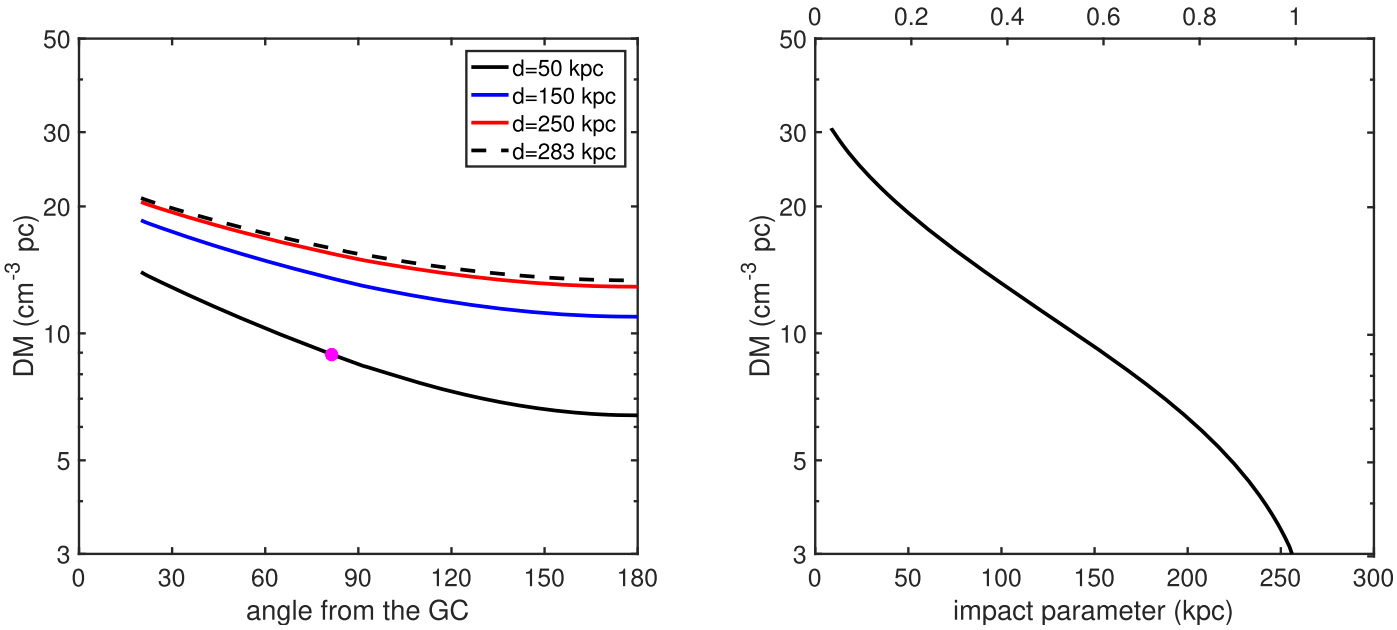

Figure 12. The DM in our model. Left: DM as a function of the angle from the GC for an observer inside the galaxy at $R_0 = 8.5$ kpc (see Section 6.1). The solid curves show the DM for sources inside the halo at distances of 50, 150, and 250 kpc from the GC. The magenta circle on the $d = 50$ kpc curve marks the angle to the LMC. Right: DM for an external observer looking through the CGM at an impact parameter h (see Section 6.2.2). The data used to create the right panel of this figure are available.

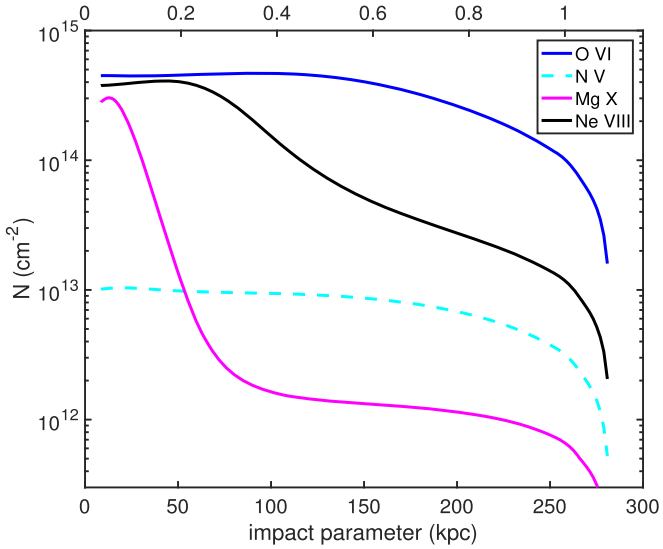

Figure 13. Predicted column density profiles for selected metal ions observable in the UV for external galaxies. The O VI and N V column density profiles (solid blue and dashed cyan) are identical to those shown in Figure 10, and measurements are available from the COS-Halos and eCGM surveys. The Ne VIII and Mg X columns (solid black and magenta, respectively) have a two-part structure, with collisional and photoionization dominating in the inner and outer parts, respectively (see Section 6.2.1). The data used to create the right panel of this figure are available.

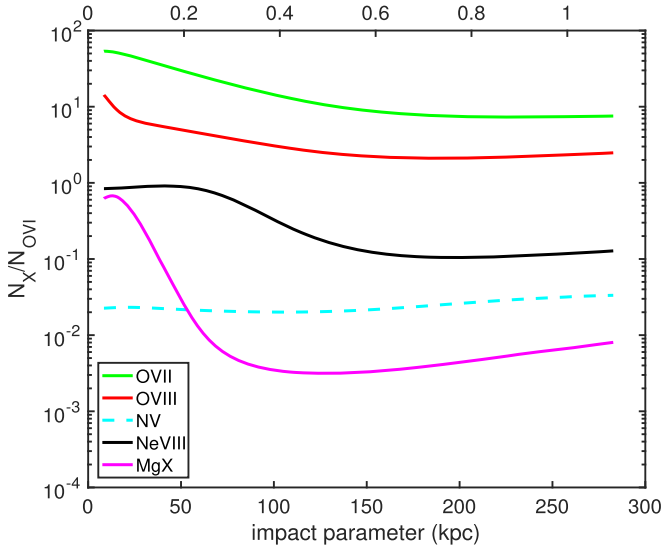

Figure 14. Predicted ratios of the ion column densities to the $N_{\rm O\,VI}$ column density profile (see Section 6.2.1). These are independent of the metallicity normalization in a specific galaxy but do depend on the shape of the metallicity profile.

Figure 13 shows the column densities of several other metal ions observable in the UV. We select N V, O VI, Ne VIII, and Mg X—ions present in gas at temperatures between $\sim 2 \times 10^5$ and 1.2×10^6 K. First, the N V and O VI profiles (dashed cyan and solid blue curves, respectively) are identical to those presented in Figure 10. As discussed in Section 5.2.1, the O VI and N V ions are abundant mainly in the outer parts of the corona (where $T_{\rm gas}$ is low), resulting in flat column density profiles. The COS-Halos N V absorption measurements give upper limits for a large fraction of the observed sight lines. We predict that the actual column densities are $\sim$(0.5–1.0) $\times$ 10^{13} cm^{-2}, a factor of 3–10 below the existing upper limits. Figure 14 shows the column density profiles of several metal ions, normalized by the OVI column density profile. These curves are independent of the mean enrichment of a specific galaxy, and can be useful for comparing to CGM absorption measurements of other galaxies. However, since various ions form at different radii in the halo, the profiles in Figure 14 do depend on the shape of the metallicity profile that we adopt in our model, given by Equation (8).

The Ne VIII and Mg X ions (solid black and magenta curves) probe hotter gas, at $T \sim 10^6$ K, and their ion fractions peak at smaller radii. Thus, their column density profiles have a two-part structure, with high columns at small impact parameters and lower values at larger (projected) distances. Current instrumentation limits observations of Ne VIII to $0.5 < z < 1.0$ (Meiring et al. 2013; Hussain et al. 2015; Burchett et al. 2019). To compare current observations with this work, we can assume that the halo and CGM properties of these higher-redshift galaxies are not very different from the MW/COS-Halos galaxies. Our model then predicts that the column density in the central part of the profile, controlled by collisional ionization of Ne VIII, will not change significantly with redshift. In the outer part of the corona, Ne VIII is created by the MGRF, and for a field intensity higher by a factor of 3–5, the column density at large impact parameters may be higher by a similar factor. Current detections of Mg X absorption are rare and at higher redshifts than our model, $z > 1.0$ (Qu & Bregman 2016).

6.2.2. X-Ray Emission and DM

The left panel of Figure 7 shows the predicted emission spectrum of the warm/hot gas in our fiducial model, and the magenta solid curve in the right panel shows the projected emission intensity profile in the 0.4–2.0 keV band. The horizontal magenta line shows the background level of 10^{35} erg s^{-1} kpc^{-2} estimated by L18 in their stacking analysis. The emission intensity in our model is above this level out to ~20 kpc. For an external observer, this would not extend much beyond the size of the MW disk and can be challenging to define clearly as CGM emission. The power-law slope of the emission profile is $a \approx 1.7$. As discussed in Section 5.1.2, the emission intensity profile may be slightly flatter for higher-mass galaxies due to the lower gas temperature and more compact mass distributions of the dark matter halos.

In the right panel of Figure 12, we show the DM as a function of the impact parameter. The DM through the CGM is $\gtrsim$20 cm^{-3} pc at impact parameters below ~50 kpc and decreases to $\lesssim$5 cm^{-3} pc at $h > 200$ kpc. For a sight line through the halo of an L^* galaxy, Prochaska & Zheng (2019) estimated a DM between 10 and 150 cm^{-3} pc for impact parameters between ~15 kpc and $r_{\rm vir}$. Scaling down the DM with the CGM mass by a factor of ~3 brings their prediction into agreement with our fiducial model (Section 6.1). Future FRB campaigns may allow one to probe the CGM of galaxies in the local universe and beyond through DM measurements (Bandura et al. 2014; McQuinn 2014).

6.2.3. SZ Effect

We calculate the spatially resolved SZ signal through the corona at an impact parameter h as

$$y(h) = \frac{\sigma_T}{m_e c^2} \int P_{\rm e,th}(r) dz = \frac{\sigma_T k_{\rm B}}{m_e c^2} \int n_{\rm e}(r) T_{\rm th}(r) dz, \quad (30)$$

where $P_{\rm e,th}$ is the electron (thermal) pressure, $n_{\rm e}$ is the electron density, and dz is the element along a line of sight. The resulting y-parameter is shown in Figure 15, and the profile decreases from $\sim 10^{-8}$ at small impact parameters to $\sim$(2–3) $\times 10^{-10}$ at $r_{\rm vir}$. Current CMB observations do not have this sensitivity, and this prediction can be compared to future spatially resolved CMB measurements of galactic halos (see Singh et al. 2015).

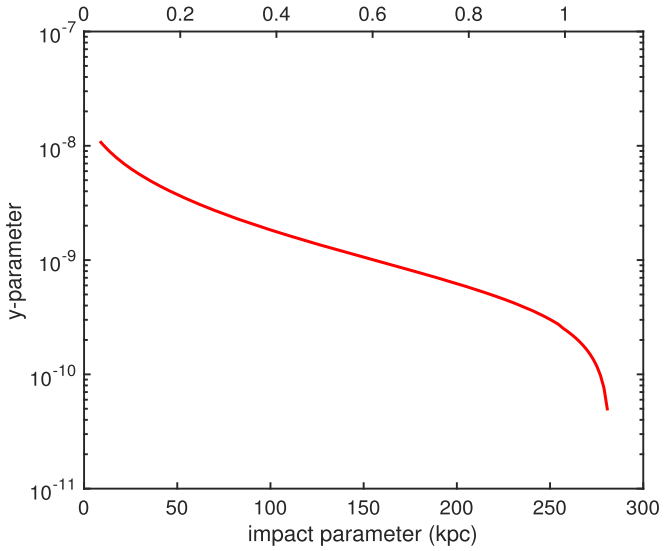

Figure 15. Predicted Compton y-parameter profile of the coronal gas in our fiducial model (see Section 6.2.3).

The Planck Collaboration et al. (2013, hereafter P13) searched for the SZ signal from gas in galaxies by stacking CMB measurements of the locally brightest galaxies. They reported the Comptonization parameter normalized to a distance of 500 Mpc, giving the intrinsic integrated SZ signal and defined as

$$\tilde{Y}_{500} \equiv \frac{\sigma_T}{m_e c^2} \frac{E^{-2/3}(z)}{(500\ {\rm Mpc})^2} \int^{R_{500}} P_{\rm e,th} dV, \quad (31)$$

where $E^2(z) = \Omega_m (1+z)^3 + \Omega_\Lambda$. The signal is calculated out to R_{500} of the halo, and $\tilde{Y}_{500}$ is usually reported in square arcminutes. We calculate it at $z = 0$, and $E(z) = 1$.

A signal from systems with stellar masses above $\sim 10^{11}\ M_\odot$ was detected by P13. For the lowest-mass bin with a 3σ detection, $M_* = 2 \times 10^{11}\ M_\odot$ ($M_{500} \sim 2 \times 10^{13}\ M_\odot$), they reported $\tilde{Y}_{500} \approx 5 \times 10^{-6}$ arcmin^2. To estimate the signal from an MW-mass galaxy,we can use the $\tilde{Y}_{500} - M_{500}$ relation, usually fit by $\tilde{Y}_{500} \propto M_{500}^{a_M}$. In their analysis, P13 adopted the slope predicted by the self-similar solution for the gas distribution in a halo of $a_M = 5/3$. Using this value to calculate the SZ signal for an MW-mass galaxy with $M_{500} \sim 7 \times 10^{11}\ M_\odot$ gives $\tilde{Y}_{500} \sim 2 \times 10^{-8}$ arcmin^2. However, P13 noted that a single power law is not a formally acceptable fit to the measured $\tilde{Y}_{500} - M_{500}$ relation. This may be a result of the gas distributions in galaxies differing from those in clusters (see also Bregman et al. 2018). Thus, the actual SZ signal for MW-mass galaxies may be different from the extrapolated value. For the MW, $R_{500} = 135$ kpc, and in our fiducial model, $\tilde{Y}_{500} = 0.5 \times 10^{-8}$ arcmin^2.

The angular resolution of the Planck maps used in the P13 stacking analysis is 10′ (FWHM; see Section 5.1 there), and the MW R_{500} will not be resolved at distances above ~50 Mpc. For spatially unresolved CMB observations, we integrate the SZ signal in our model out to $r_{\rm CGM}$ and get $\tilde{Y} = 1.2 \times 10^{-8}$ arcmin^2. This is similar to the estimate by Singh et al. (2015) of $\tilde{Y}_{500} \sim 10^{-8}$ arcmin^2 for the warm, O VI-bearing CGM.

7. Comparison to FSM17

We now address the similarities and differences between our isentropic corona described in this work and our isothermal model presented in FSM17.

Starting with the similarities, both models require significant nonthermal support to reproduce the observed O VI column density profile. For isothermal, the ratio of total to thermal pressure is independent of radius, with a value of $\alpha \approx 2$. For isentropic, the ratio varies with radius between $\alpha(r_{\rm CGM}) \approx 3$ and $\alpha(R_0) \sim 1.5$. The result of the nonthermal support is that the gas density profiles have shallow slopes with similar power-law indices of 0.93 and ≈0.90 in the isentropic and isothermal models, respectively. The extent of the CGM in both models is similar, with 280 and 250 kpc, as suggested by the O VI absorption studies of $\sim L^*$ galaxies in the low-redshift universe.

The two models differ in several important aspects. First are the gas temperature distributions. In FSM17, we included a local (isobaric) lognormal distribution of temperature (and density), but the local mean gas temperature does not vary with radius. In our isentropic model, locally, the gas has a single temperature, but it decreases from $\sim 2 \times 10^6$ K at R_0 to $T_{\rm vir} \sim 2 \times 10^5$ K at $r_{\rm CGM}$. The temperature variation results from adopting the adiabatic EoS, with $T \propto \rho^{\gamma-1}$ and constant entropy.

Second, the mean gas density in our isentropic corona is a factor of ∼3 lower than in FSM17, and the total gas mass inside $r_{\rm vir}$ is also lower by a similar factor. With a baryonic overdensity of ∼20, this is closer to the values predicted by structure formation theory. As a result of the lower density and temperature, the total pressure at the outer boundary is ∼20 K cm^{-3}, ∼10 times lower than that in our isothermal model and similar to the IGM pressure in cosmological simulations. The pressure in the inner part of our isentropic model is also lower, with $P/k_{\rm B} = 1350$ K cm^{-3}, compared to 2200 K cm^{-3} in the isothermal model.

For the higher gas densities in FSM17, pure CIE is a good approximation, and photoionization by the MGRF has a negligible effect on the gas ionization state. In our isentropic model, the gas density at large distances from the galaxy is low enough for photoionization to reduce the ion fractions of the N V and O VI ions. For other ions, O VII and O VIII, radiation may increase the fractions locally in some parts of the corona but does not have a significant effect on the total column densities for an observer inside the Galaxy.

In FSM17, the gas metallicity is constant, with $Z' = 0.5$ solar, while in our current model, we adopt a varying metallicity profile. This is motivated by enrichment of the CGM by the Galaxy through outflows and metal mixing, and in our fiducial model, the metallicity varies from $Z'(R_0) = 1.0$ to $Z'(r_{\rm CGM}) = 0.3$. The combination of temperature and metallicity gradients leads to shorter length scales for O VII and O VIII (see Section 5.1.1). Furthermore, in FSM17, the O VII and O VIII ions had the same half-column length scale for an observer inside the galaxy. The temperature gradient in the isentropic model leads to a different spatial distribution of these ions: the O VII is more extended, while the O VIII is more compact (see Figure 11 and Table 2).

Finally, in both FSM17 and this work, the origin of the O VI is in warm, collisionally ionized gas. However, the properties of this gas in the two models are different. In our isothermal corona, the warm gas is a separate phase that condenses out of the hot, 2×10^6 K, gas. Since we assume the two phases are in pressure equilibrium, the warm gas density is higher than in the hot phase. This, together with its higher cooling rate, leads to short cooling times of $t_{\rm cool} \sim 2 \times 10^8$ yr (without heating). In our isentropic model, the O VI is formed in virialized gas at lower densities. The combination of the lower gas density and metallicity leads to a longer cooling time, with $t_{\rm cool} \geqslant 3 \times 10^9$ yr at $r > 100$ kpc, and this gas can be long-lived even without constant energy injection. Furthermore, the total luminosity of the isentropic corona is lower by ∼20, and the radiative losses per gas unit mass are 10 times lower. Similar to the isothermal model, we assume a stable heating/cooling equilibrium in our current model.

8. Discussion

Many recent works studied the CGM in detailed simulations of galaxy formation and evolution. Oppenheimer et al. (2016) addressed the origin of the O VI–SFR correlation in the EAGLE simulation suite, and Hafen et al. (2019) studied the properties of the CGM in the FIRE simulations. Nelson et al. (2018) explored the distribution of highly ionized oxygen (O VI–O VIII) in the "Illustris" cosmological simulation, and Roca-Fàbrega et al. (2019) focused on the evolution of O VI with redshift in zoom-in simulations. Li & Tonnesen (2019) examined the impact of SN-driven outflows on the structure of the CGM. Hummels et al. (2019) and Peeples et al. (2019) used zoom-in simulations to check how numerical resolution affects the CGM properties. In this section, we compare our model to recent analytical models of the CGM.

Miller & Bregman (2013, hereafter MB13) fit the observed O VII and O VIII column densities for a constant temperature. They assumed a power-law radial density distribution and found a best-fit power-law index of $a_{\rm n} \sim 1.7$. They adopted $r_{\rm CGM} = r_{\rm vir} = 200$ kpc and got a total CGM mass of $1.2^{+1.7}_{-0.2} \times 10^{10}\ M_\odot$. There are two caveats to this estimate. First, the value they adopted for the virial radius is smaller than what is usually taken for the MW, with $r_{\rm vir} \sim 250$ kpc for a halo of $\sim 1.5 \times 10^{12}\ M_\odot$ (see Table 8 in Bland-Hawthorn & Gerhard 2016). Second, the mean hydrogen density inside 200 kpc is 1.1×10^{-5} cm^{-3}, lower than the estimate by BR00 for $r < 250$ kpc, with $\sim 2.5 \times 10^{-5}$ cm^{-3}. This discrepancy was addressed by MB13 by adding an "ambient" component with a constant density of $n_{\rm e} = 10^{-5}$ cm^{-3} and saying that its mass is within their mass uncertainty. We now reestimate the MB13 gas mass to compare it to our model. A constant density component with $r = 258$ kpc and $n_{\rm e} = 10^{-5}$ cm^{-3} has a total mass of $2.0 \times 10^{10}\ M_\odot$. Scaling the intrinsic gas mass by a factor of $(258/200)^{1.3} \approx 1.4$ (since $n \propto r^{-1.7}$) and summing the two components gives a total mass of $\sim 3.6 \times 10^{10}\ M_\odot$. This is closer to the warm/hot gas mass inside $r_{\rm vir}$ in our fiducial model, with $4.6 \times 10^{10}\ M_\odot$. This calculation shows the sensitivity of the result to the value of $r_{\rm CGM}$ and the importance of density constraints at large distances from the MW for estimates of the total CGM mass. Furthermore, the apparent difference between the initial steep profile of the MB13 fit, inferred from the X-ray absorption measurements, and the density estimate of BR00 may be evidence for lower CGM temperatures at larger distances from the Galaxy.

Qu & Bregman (2018, hereafter QB18a) and Qu & Bregman (2018, hereafter QB18b) constructed a CGM model for halos with masses between 3×10^{10} and $2 \times 10^{13}\ M_\odot$. In their model, the temperature is constant as a function of radius. They

assumed a virial temperature of $T_{\rm vir} \sim 7 \times 10^5$ K for a 10^{12} $M_\odot$ halo, a factor of ∼3 higher than the temperature of the shocked gas at $r_{\rm CGM}$ in our fiducial model. They consider two main model versions: (i) an isothermal model with a single temperature at each radius (with and without radiation) and (ii) a model with a local temperature/density distribution function that is proportional to the gas cooling time.

For their fiducial galaxies, QB18a assumed a power-law density profile with a slope of 1.5 and a constant metallicity of $Z' = 0.3$ solar and calculated the column densities through the CGM for several high metal ions: O VI–O VIII, Ne VIII, and Mg X. For MW-mass halos, they got $N_{\rm O\,VI} \sim 5 \times 10^{13}$ cm^{-2} at an impact parameter of $h/r_{\rm vir} = 0.3$ (see their Figure 5), and including photoionization reduces the O VI column, similar to the effect in our model. Adopting a local temperature distribution increases the O VI column to $\sim 1.5 \times 10^{14}$ cm^{-2}, still below the values observed by COS-Halos. To fit the O VI–O VIII columns observed in the MW, QB18a constructed a different model with a higher metallicity of $Z' = 0.5$–1.0 and $T_{\rm vir} \sim 2 \times 10^6$ K. Thus, the gas temperature inferred by QB18a for the MW is higher by a factor of ∼2–3 than that of their fiducial galaxies at similar halo masses. The temperature of the hot phase and the gas metallicity in our FSM17 model are similar to the QB18a MW fit. However, in our analysis, other MW-like galaxies in the low-redshift universe have similar values for these properties.

The total gas mass in the QB18a fiducial models is low compared to the stellar mass of these galaxies, with $M_{\rm CGM} \sim (1$–$2) \times 10^{10}$ $M_\odot$ for a 10^{12} $M_\odot$ halo (see their Figure 18). Including the stellar mass gives an almost constant baryon fraction for halos with $M_{\rm halo} > 5 \times 10^{11}$ $M_\odot$, with $f_{\rm b} \approx 0.05$–0.06, or 30%–40% of the cosmic budget. Given the density profile, extending the CGM distribution to twice the virial radius increases the coronal gas mass only by a factor of 2–3. For these CGM masses, the mean coronal gas density inside the virial radius is small, with $\langle n_{\rm H} \rangle \sim 10^{-5}$ cm^{-3}, and the actual density at large radii is lower by a factor of ∼3. This is similar to the problem discussed by MB13 for their model. A similar solution, adding an ambient, constant density component, will increase the total gas mass and result in a gas density profile with an effective shallower slope. A key difference between our models (isothermal and isentropic) and MB13/QB18a is the slope of the density profile. Our models have flatter profiles that result from including nonthermal pressure support.

Stern et al. (2018, hereafter S18) constructed a two-zone model for the CGM with the two regions separated by the virial shock located at $r_{\rm shock} \approx 0.6\ r_{\rm vir}$. The inner CGM consists of hot gas at $T \sim 5 \times 10^5$ K, and the outer part is cool, photoionized gas at $T = 3 \times 10^4$ K. In this model, O VI is formed in the cool, photoionized gas outside $r_{\rm shock}$.

Voit (2019, hereafter V19) presented CGM models with gas in HSE and entropy that increases as a function of radius. We now compare the properties of his fiducial model (named pNFW/Zgrad) and our isentropic model. The dark matter halo of the pNFW model has a isothermal core and an outer NFW part. The gas distribution at small radii has a constant cooling to a dynamical time ratio of $t_{\rm cool}/t_{\rm dyn} = 10$ (or higher), motivated by precipitation-limited models (see also Voit et al. 2018). The gas density behaves as $n \propto r^{-1.2}$ at small radii, similar to our density slope. At large radii, the gas density profile steepens, with $n \propto r^{-2.3}$. The gas density range between 30 and ∼250 kpc is similar to ours (see their Figure 1), and the total CGM mass inside $r_{200} \approx 261$ kpc is 5×10^{10} $M_\odot$. The gas metallicity profile in pNFW/Zgrad is also similar to ours, decreasing from $Z/Z_\odot = 1.0$ in the vicinity of the disk to 0.3 in the outer halo.

The gas temperatures in the pNFW model are $T \sim 8.5 \times 10^5$ K at r_{200} and $\sim 3 \times 10^6$ K at ∼10 kpc, higher than in our fiducial model. As a result, the O VII/O VIII column ratio in this model is ∼1 for an observer inside the galaxy, lower than estimated for the MW CGM, ∼4 (see Table 2). Furthermore, the O VI column densities for an external observer are $<10^{14}$ cm^{-2}, lower than measured in the COS-Halos survey. To solve this, V19 invoked local temperature fluctuations (as we introduced in FSM17 2017) and showed that a wide distribution (0.3–0.4 dex) can increase the O VI fractions and columns by a factor of up to ∼5.

In his calculations of the ion fractions for the MW, V19 assumes CIE and predicts that in lower-mass halos, O VI will be created by photoionization. We check this by scaling down the temperature at r_{200} in his MW model to $M_{\rm halo} = 3 \times 10^{11}$ $M_\odot$, which gives $T(r_{200}) = 8.5 \times 10^5\,{\rm K}(3 \times 10^{11}/2 \times 10^{12})^{2/3} \approx 2.5 \times 10^5$ K, just below the O VI peak. As we show in Section 3.2 (Figures 5 and 6), at this temperature and densities of 10^{-5}–10^{-4} cm^{-3} (or pressures of $P/k_{\rm B} \sim 2$–20 K cm^{-3}), photoionization already reduces the O VI fraction to $f_{\rm O\,VI} \approx 0.1$. At higher temperatures, for halo masses between 3×10^{11} and 2×10^{12} $M_\odot$, the O VI will be even lower. Photoionization will increase the O VI fraction for lower temperatures at the outer boundary, at $T \lesssim 2 \times 10^5$ K and $n_{\rm H} < 10^{-4}$ cm^{-3}.

In the V19 framework, the gas density in the inner region of the CGM is regulated by its cooling time, so that $t_{\rm cool}/t_{\rm dyn}$ is above some threshold value, chosen to be 10 or higher. We note that in our isentropic model, the same result is obtained naturally; the gas temperature in the inner part is high ($\sim 2 \times 10^6$ K), and the dynamical time is low, leading to $t_{\rm cool}/t_{\rm dyn} > 10$ at $r < 30$ kpc (see Figure 8). However, the ratio is different in the two models at large radii, ∼200 kpc, with $t_{\rm cool}/t_{\rm dyn} \sim 10$ in V19 and ∼3 in our isentropic model, consistent with the upper limit (see Section 4.1). The gas densities and metallicities are similar (for pNFW/Zgrad), and the reason for this difference is the gas temperature. In our model, we set the temperature at $r_{\rm CGM}$ to be roughly the virial gas temperature at that radius, which happens to be close to the peak in the gas cooling efficiency, at $\sim 3 \times 10^5$ K. Here V19 chose $T(r_{200}) \approx 8.5 \times 10^5$ K, where the cooling efficiency of the gas is lower by a factor of 2–3 and the cooling time is long.

The gas properties in our model are similar to those of the MW-mass (10^{12} $M_\odot$) halo in the idealized simulations by Fielding et al. (2017, hereafter F17). The gas densities between $0.1\ r_{\rm vir}$ and $r_{\rm vir}$ are in the range of 10^{-5}–4×10^{-3} cm^{-3}, and the CGM temperature is in the range of 3×10^5–2×10^6 K (see their Figure 7), similar to the densities and temperatures in our model. It was found by F17 that for a 10^{12} $M_\odot$ halo, the feedback strength does not affect the CGM properties outside the central part of the halo (at $r/r_{\rm vir} < 0.1$). Lochhaas et al. (2020) analyzed these simulations and found that when turbulent support is included, the CGM at large radii is close to HSE. The density profile in the simulated CGM is steeper than ours, with $a_{\rm n} \sim 1.5$. However, the simulations do not include feedback from the central black hole, magnetic fields, and cosmic rays. We have shown that nonthermal pressure support is important for reproducing the observed O VI column

density profile. This is especially true at large radii in our isentropic model, where the value of α increases with distance from the Galaxy. Recent simulations also show that cosmic-ray pressure is significant in MW-mass halos at $z < 1$ (Salem et al 2016; Ji et al. 2019; Kempski & Quataert 2020).

These comparisons uncover an interesting point. Models of MW-sized halos that adopt gas temperatures of $\sim 10^6$ K produce O VI column densities of $\sim 10^{14}$ cm^{-2}, a factor of 3–5 lower than measured by COS-Halos in $z \sim 0.2$ galaxies. One solution for this is to invoke temperature fluctuations, as we did in FSM17, and V19 found that wide distributions are required to reproduce the observed O VI. In our current model, the gas temperature at the outer CGM boundary is lower than the values adopted by QB18a and V19. This gives high O VI columns without local temperature distributions. We emphasize that the warm/hot CGM undoubtedly has some temperature fluctuations, and such fluctuations were important in the FSM17 model.[16] In the present model, we have chosen to omit them, since they add an additional parameter and do not affect our model significantly unless they are larger than those in FSM17, which were about 0.15 dex. To summarize, the two main suggested mechanisms for creating high $N_{\rm O\,VI}$ in warm/hot gas are (i) a global variation in gas temperature, with $T \sim 3 \times 10^5$ K at the outer boundary, and (ii) a wide local temperature distribution in $T \sim 10^6$ K gas. Stern et al. (2018) suggested a different scenario, in which the O VI is created in low-density, cool, photoionized gas outside the virial shock.

9. Summary

In this paper, we present a new phenomenological isentropic model for the CGM of L^*, MW-like galaxies. Our model reproduces a wide range of absorption measurements in the UV and X-ray of the MW and the $0.1 < z < 0.4$ galaxies observed in the COS-Halos/eCGM surveys. We assume that the CGM is in HSE and adopt an adiabatic EoS for the virialized gas, which results in a temperature variation as a function of radius (see Figure 1). We also introduce a decreasing metallicity profile motivated by gas enrichment of the CGM by the galaxy (Section 2).

In Section 3 we described our fiducial corona, defined by a specific set of parameters chosen to reproduce the highly ionized oxygen observations in absorption (see Table 1). The gas density and pressure at the outer boundary of the corona, $r_{\rm CGM} \approx 283$ kpc, are low, with $n_{\rm H} \sim 10^{-5}$ cm^{-3} and $P_{\rm tot}/k_{\rm B} \sim 20$ K cm^{-3}, consistent with a picture of a (quasi-) static corona. The total gas mass inside the virial radius ($r_{\rm CGM}$) is 4.6×10^{10} (5.5×10^{10}) $M_\odot$. Together with the Galactic disk, this constitutes $\sim$70% of the galactic baryonic budget of the MW.

Our model is tuned to reproduce the O VI–O VIII absorption observations, and these do not directly constrain the total gas mass. In our model, a given temperature distribution sets the density profile shape, and the gas mass is then proportional to the density at the outer boundary or the pressure at the solar radius. The ion fractions are also set by the temperature, and for a fixed value of $r_{\rm CGM}$, the column densities constrain the product of the gas metallicity and density (or pressure). However, each of these properties individually can vary, and we scale the CGM mass in our model with $P/k_{\rm B} = 1350$ K cm^{-3} at the solar circle, R_0, to the observationally estimated range of $\sim$1000–3000 K cm^{-3} (see Section 2.3). This results in (0.34–1.0) $\times 10^{11}$ $M_\odot$ for the gas mass inside $r_{\rm vir}$ or, including the disk mass, between 60% and 100% of the Galactic baryonic budget for a 10^{12} $M_\odot$ halo. Cool, $\sim 10^4$ K, gas may be an additional significant component.

For the gas densities and pressures in our fiducial model, photoionization by the MGRF affects the metal ion fractions (Section 3.2). This is in contrast to the FSM17 model, where, due to the higher gas densities and temperatures, pure CIE was a valid assumption. In our calculations, we include the effect of the MGRF on the ion fractions and cooling functions and adopt the HM12 field at $z = 0.2$, the median redshift of the COS-Halos galaxies.

We derive a model-independent upper limit on the cooling time of O VI-bearing warm/hot gas in Section 4, with the detailed calculation presented in the Appendix. We show that for the typical column density measured in the COS-Halos survey, $N_{\rm O\,VI} \approx 3 \times 10^{14}$ cm^{-2}, the cooling time at large radii in the CGM ($r/r_{\rm vir} \sim 0.6$) is less than 5.6×10^9 yr. For an MW-mass halo, this results in a ratio of $\lesssim$4 for the cooling to dynamical times, below the value of $\approx$10 estimated in previous works for galaxy clusters and invoked in precipitation models for the CGM. This suggests that cool gas may form by condensation out of the warm/hot phase, in agreement with observations of low metal ions in the CGM, and we address these in our next paper. In our fiducial model, $t_{\rm cool}/t_{\rm dyn} \sim 2.5$ at $r > 100$ kpc, consistent with the limit we derive. Our equilibrium model assumes that most of the radiative losses are offset by heating of the CGM, requiring an energy input of $\sim 8 \times 10^{40}$ erg s^{-1}. The total (thermal, nonthermal, and turbulent) energy in our fiducial corona model is $\sim 2.5 \times 10^{58}$ erg, similar to the energy radiated at the present-day luminosity over $\sim$10 Gyr. We estimate that the total energy available over this epoch in the MW from SMBH feedback, SN events, and IGM accretion is $\sim 2.5 \times 10^{59}$ erg, a factor of $\sim$5 higher than needed to form and balance the radiative losses of the CGM.

We compare our model to existing CGM observations in Section 5. It reproduces the O VI column density profile of the COS-Halos/eCGM galaxies (Figure 10) and the O VII–O VIII columns measured in the MW (Table 2). The N V column densities in the model are $\sim 10^{13}$ cm^{-2}, a factor of $\sim$5 below the upper limits reported in COS-Halos. Our computed DM, DM = 8.8 pc cm^{-3}, is consistent with the estimated upper limit of $\lesssim$23 pc cm^{-3} to the LMC. The X-ray emission intensities in the model constitute $\sim$20% of the values measured in the MW. Reproducing these requires high pressure at the solar radius, $\sim$4500 K cm^{-3}. As shown in FSM17, a Galactic disk origin may be a plausible explanation for this emission.

Finally, in Section 6, we present the predictions of our model for future observations in the UV and X-ray. We calculate the column densities of different metal ions (N V, Ne VIII, Mg X, etc.) and the emission intensity profiles in different energy bands. We find that in the X-ray, the emission detected today may be very compact due to instrumental sensitivity and backgrounds. We show predicted profiles for the CGM DM for pulsar and FRB observations and the Compton y-parameter for measurements of the SZ effect. We plot our predictions as a

[16] In FSM17, we invoked isobaric temperature/density fluctuations in the gas, which resulted in shorter cooling times for a fraction of the hot gas mass ($\sim$20%) and provided a physical mechanism for the formation of the warm, O VI-bearing phase. The small fluctuations had a minor effect on the actual ion fractions and column densities.

function of the angle from the GC for the MW and the impact parameter through the CGM for external galaxies. We hope these will be useful for testing our model, improving our understanding of the CGM, and studying the physical processes that shape its structure and evolution.

The manuscript is accompanied by two data files in machine-readable format. The files list the model properties and outputs as a function of radius and impact parameter to allow comparison to models and observations. The provided data were used to produce Figures 1–3, 6–9, and 11–15.

We thank Yuval Birnboim, Greg Bryan, Avishai Dekel, Drummond Fielding, Shy Genel, Orly Gnat, Jerry Ostriker, Kartick Sarkar, David Spergel, and Jonathan Stern for fruitful discussions and helpful suggestions during the course of this work. We thank Joss Bland-Hawthorn, Sebastiano Cantalupo, Filippo Fraternali, Aryeh Maller, Smita Mathur, Mike Shull, Benny Trakhtenbrot, and the anonymous referee for helpful comments on the manuscript.

This research was supported by the Israeli Centers of Excellence (I-CORE) program (center No. 1829/12), the Israeli Science Foundation (ISF grant No. 857/14), and DFG/DIP grant STE 1869/2-1 GE625/17-1. C.F.M. is supported in part by HST grant HST-GO-12614.004-A. C.F.M. and Y.F. thank the Center for Computational Astrophysics and the Flatiron Institute, Simons Foundation, where some of this research was carried out with A.S., for hospitality and funding.

Appendix
Cooling to Dynamical Time Ratio of O VI-bearing Gas

In this Appendix, we present a full derivation of our analytical estimate for the cooling time of O VI-bearing gas and derive an upper limit for the ratio of cooling to dynamical time for an MW-mass galaxy. We argue that the O VI columns observed in the COS-Halos survey by Tumlinson et al. (2011a) imply cooling to dynamical time ratios significantly lower than estimated in galaxy clusters by Voit et al. (2017).

A.1. Ion Column Density

The column density of ion i at an impact parameter h in a spherically symmetric halo is

$$N_i(h) = 2A_{\rm i}\int_0^z n_{\rm H}(r)Z'(r)f_V(r)f_{\rm ion,i}(r)dz', \tag{A1}$$

where $r^2 = h^2 + z^2$, $A_{\rm i}$ is the solar abundance of the element corresponding to ion i, Z' is the metallicity relative to solar, f_V is the volume-filling factor of the gas containing ion i, and $f_{\rm ion,i}$ is the ion fraction. We assume a power-law variation of the density, $n_{\rm H} \propto r^{-a_n}$; metallicity, $Z' \propto r^{-a_Z}$; filling factor, $f_V \propto r^{-a_V}$; and ion fraction, $f_{\rm ion,i} \propto r^{-a_f}$. We then have

$$N_i(h) = 2A_{\rm i}f_{\rm ion,i}(h)n_{\rm H}(h)Z'(h)f_{\rm V}(h)\int_0^z \frac{dz'}{(r/h)^a}, \tag{A2}$$

where $n_{\rm H}(h) = n_{\rm H}(r = h)$, etc., and $a = a_n + a_Z + a_V + a_f$ ($a > 0$). Let

$$y' \equiv \frac{z'}{h} = \left(\frac{r^2}{h^2} - 1\right)^{1/2}, \tag{A3}$$

and let R be the virial radius of the Galaxy, close to the outer radius of the CGM. We then define

$$I_a(y) \equiv \frac{1}{R}\int_0^z \frac{dz'}{(r/h)^a} = \frac{1}{(1+y^2)^{1/2}}\int_0^y \frac{dy'}{(1+y'^2)^{a/2}} \tag{A4}$$

and get

$$N_i(h) = 2A_{\rm i}f_{\rm ion,i}(h)n_{\rm H}(h)Z'(h)f_{\rm V}(h)RI_a. \tag{A5}$$

If we restrict our attention to normalized impact parameters in the range $0.3 < h/R < 0.9$, which contains most of the COS-Halos measurements (see Figure 10), then for a between 1 and 2, $I_a = 0.50 \pm 0.13$ dex (or 0.50 ± 0.18 dex for $a = 0.5$–2.5).

A.2. Limit on the Cooling Time

Let the rate of radiative net cooling per unit volume be $n_{\rm e}n_{\rm H}\Lambda$. We assume that the gas is irradiated by the MGRF. The cooling function, Λ, is then a function of the gas density, temperature, and metallicity (see Section 4 and Gnat 2017). The isochoric gas cooling rate is then

$$t_{\rm cool} = \frac{3nk_{\rm B}T}{2n_{\rm e}n_{\rm H}\Lambda(T, n, Z)}, \tag{A6}$$

where we have adopted $n_{\rm He} = n_{\rm H}/12$ and assumed that the gas is fully ionized. For the metallicity scaling, $\Lambda = Z'\Lambda_\odot$, we neglect cooling due to H and He, so this an upper limit on the cooling time. Inserting the expression for $n_{\rm H}(h)Z'(h)$ from Equation (A5), we get

$$t_{\rm cool}(h) = 5.8A_{\rm i}f_{\rm V}(h)\left[\frac{k_{\rm B}T(h)f_{\rm ion,i}(h)}{\Lambda_\odot(T, n)}\right]\frac{RI_a}{N_i(h)}. \tag{A7}$$

In this expression, the uncertain metallicity Z does not appear, and the cooling time is inversely proportional to the observable column density.

We now apply this to O VI. We assume that the warm/hot gas is volume-filling, so that $f_{\rm V} = 1$ and $a_{\rm V} = 0$. This gives an upper limit for the cooling time, consistent with the rest of our analysis here. The filling factor of the warm/hot, O VI-bearing gas in our model is unity. The solar abundance of oxygen is $A_{\rm O} = 4.9 \times 10^{-4}$, and as we estimated above, $I_a \approx 0.50$. For our estimate here, we take $R = 260$ kpc, the median virial radius of the COS-Halos SF galaxies, and close to the MW virial radius in our model (see Section 3). Given the shape of the cooling function and the O VI ion fraction in the density–temperature space, the expression $k_{\rm B}Tf_{\rm ion,i}/\Lambda_\odot$ is bound from above for gas at $T > 10^5$ K. For the HM12 MRGF at $z = 0.2$, $k_{\rm B}Tf_{\rm ion,OVI}/\Lambda_\odot \leqslant 4.6 \times 10^{10}$ s cm^{-3}, and the maximum occurs at $T \sim 3.5 \times 10^5$ K at densities above $n_{\rm H} \geqslant 10^{-4}$ cm^{-3}, where the O VI is in CIE and $f_{\rm ion,OVI}$ is maximal (see Section 3.2). We insert this value into Equation (A7) to obtain a model-independent upper limit for the cooling time at $r = h$:

$$t_{\rm cool}(r = h) \lesssim 5.6\ {\rm Gyr}\left(\frac{R}{260\ {\rm kpc}}\right)\left(\frac{N_{\rm O\,VI}(h)}{3 \times 10^{14}\ {\rm cm}^{-2}}\right)^{-1}. \tag{A8}$$

This approximation is valid for $0.3 < h/R < 0.9$ through $N_{\rm O\,VI}(h)$, and we scaled the column density to the value measured in COS-Halos at $h/R \sim 0.6$ (see Figure 10).

A.3. Comparison with the Dynamical Time

The dynamical time used by Voit et al. (2017) is $\sqrt{2r/g(r)}$, where $g(r)$ is the acceleration due to gravity. Scaling gives

$$t_{\rm dyn}(r) = 2.8\ {\rm Gyr}\left(\frac{r}{260\ {\rm kpc}}\right)^{3/2}\left(\frac{M(r)}{10^{12}\ M_\odot}\right)^{-1/2}. \quad \text{(A9)}$$

We can fit the Klypin MW-mass profile at large radii, where it is approximately an NFW profile, with a power law, giving

$$M(r) \approx 10^{12}\ M_\odot \left(\frac{r}{260\ {\rm kpc}}\right)^{0.56} (130\ {\rm kpc} < r < 260\ {\rm kpc}). \quad \text{(A10)}$$

Inserting this into Equation (A9) results in

$$t_{\rm dyn}(r) \approx 2.8\ {\rm Gyr}\left(\frac{r}{260\ {\rm kpc}}\right)^{1.22}. \quad \text{(A11)}$$

We note that, unlike our expression for the cooling time upper limit, this approximation for $t_{\rm dyn}$ is valid all the way out to R.

We can then define $\zeta(r) \equiv t_{\rm cool}(r)/t_{\rm dyn}(r)$ and write the upper limit of this ratio for the typical column of O VI as

$$\zeta(r = h) < 2.0\left(\frac{h}{260\ {\rm kpc}}\right)^{-1.22}\left(\frac{N_{\rm O\ VI}(h)}{3\times 10^{14}\ {\rm cm^{-2}}}\right)^{-1}. \quad \text{(A12)}$$

Accounting for the uncertainty factor in the value of I_a gives ratios in the range of 1.5–2.6 for $1 < a < 2$, corresponding to a factor of 1.3 uncertainty; for $0.5 < a < 2.5$, the range is 1.3–3.0, or a factor of 1.5 uncertainty. Our approximation and the derived upper limit are valid for $0.3 < h/R < 0.9$, and the column density we used is measured at $h/R = 0.6$, corresponding to $h = 156$ kpc. Inserting this impact parameter, we get an observed upper limit $\zeta < 3.7$ (in the range 2.8–4.8 for $1 < a < 2$). This is significantly lower than values of $\zeta \sim 10$ found by Sharma et al. (2012b) in simulations and Voit et al. (2017) in observations of galaxy clusters.

To summarize, we find that for warm/hot gas with an O VI column density of $\sim 3\times 10^{14}$ cm^{-2} at large impact parameters, observations set an upper bound $\zeta \lesssim 5$. This limit includes the uncertainty in the underlying ion volume density distribution. It is also independent of the exact gas metallicity, as long as the gas cooling in the relevant temperature range is dominated by metals ($Z' \gtrsim 0.1$). A ratio $\zeta \sim 10$ would require O VI columns significantly lower than observed in the CGM of L^* galaxies.

ORCID iDs

Yakov Faerman https://orcid.org/0000-0003-3520-6503
Christopher F. McKee https://orcid.org/0000-0003-1858-3892

References

Anderson, M. E., & Bregman, J. N. 2010, ApJ, 714, 320
Armillotta, L., Fraternali, F., & Marinacci, F. 2016, MNRAS, 462, 4157
Asplund, M., Grevesse, N., Sauval, A. J., & Scott, P. 2009, ARA&A, 47, 481
Bandura, K., Addison, G. E., Amiri, M., et al. 2014, Proc. SPIE, 9145, 914522
Birnboim, Y., & Dekel, A. 2003, MNRAS, 345, 349
Bland-Hawthorn, J., & Gerhard, O. 2016, ARA&A, 54, 529
Bland-Hawthorn, J., Maloney, P. R., Stephens, A., et al. 2017, ApJ, 849, 51
Blitz, L., & Robishaw, T. 2000, ApJ, 541, 675
Bower, R. G., Schaye, J., Frenk, C. S., et al. 2017, MNRAS, 465, 32
Bregman, J. N. 2007, ARA&A, 45, 221
Bregman, J. N., Anderson, M. E., Miller, M. J., et al. 2018, ApJ, 862, 3
Bregman, J. N., & Lloyd-Davies, E. J. 2007, ApJ, 669, 990
Burchett, J. N., Tripp, T. M., Prochaska, J. X., et al. 2019, ApJL, 877, L20
Cantalupo, S. 2010, MNRAS, 403, L16
Crawford, F., Kaspi, V. M., Manchester, R. N., et al. 2001, ApJ, 553, 367
Das, S., Mathur, S., Gupta, A., et al. 2019, ApJ, 885, 108
Das, S., Mathur, S., Nicastro, F., et al. 2019, ApJL, 882, L23
Dedes, L., & Kalberla, P. W. M. 2010, A&A, 509, A60
Dutton, A. A., & Macciò, A. V. 2014, MNRAS, 441, 3359
Faerman, Y., Sternberg, A., & McKee, C. F. 2013, ApJ, 777, 119
Faerman, Y., Sternberg, A., & McKee, C. F. 2017, ApJ, 835, 52
Fang, T., Buote, D., Bullock, J., & Ma, R. 2015, ApJS, 217, 21
Faucher-Giguère, C.-A. 2020, MNRAS, 493, 1614
Ferland, G. J., Chatzikos, M., Guzmán, F., et al. 2017, RMxAA, 53, 385
Fielding, D., Quataert, E., Martizzi, D., et al. 2017, MNRAS, 470, L39
Fielding, D., Quataert, E., & Martizzi, D. 2018, MNRAS, 481, 3325
Fielding, D., Quataert, E., McCourt, M., & Thompson, T. A. 2017, MNRAS, 466, 3810
Gatto, A., Fraternali, F., Read, J. I., et al. 2013, MNRAS, 433, 2749
Genel, S., Vogelsberger, M., Springel, V., et al. 2014, MNRAS, 445, 175
Gnat, O. 2017, ApJS, 228, 11
Gnat, O., & Sternberg, A. 2007, ApJS, 168, 213
Gravity Collaboration, Abuter, R., Amorim, A., et al. 2019, A&A, 625, L10
Grcevich, J., & Putman, M. E. 2009, ApJ, 696, 385
Gupta, A., Mathur, S., Krongold, Y., Nicastro, F., & Galeazzi, M. 2012, ApJL, 756, L8
Haardt, F., & Madau, P. 2012, ApJ, 746, 125
Hafen, Z., Faucher-Giguère, C.-A., Anglés-Alcázar, D., et al. 2019, MNRAS, 488, 1248
Henley, D. B., & Shelton, R. L. 2010, ApJS, 187, 388
Henley, D. B., Shelton, R. L., Kwak, K., Joung, M. R., & Mac Low, M.-M. 2010, ApJ, 723, 935
Hummels, C. B., Smith, B. D., Hopkins, P. F., et al. 2019, ApJ, 882, 156
Hussain, T., Muzahid, S., Narayanan, A., et al. 2015, MNRAS, 446, 2444
Ji, S., Chan, T. K., Hummels, C. B., et al. 2019, arXiv:1909.00003
Johnson, S. D., Chen, H.-W., & Mulchaey, J. S. 2015, MNRAS, 449, 3263
Johnson, S. D., Mulchaey, J. S., Chen, H.-W., et al. 2019, ApJL, 884, L31
Joung, M. R., Putman, M. E., Bryan, G. L., et al. 2012, ApJ, 759, 137
Kaastra, J., Finoguenov, A., Nicastro, F., et al. 2013, arXiv:1306.2324
Keane, E., Bhattacharyya, B., Kramer, M., et al. 2015, in Advancing Astrophysics with the Square Kilometre Array (AASKA14), 40 (Trieste: SISSA)
Kempski, P., & Quataert, E. 2020, MNRAS, 493, 1801
Klypin, A., Zhao, H., & Somerville, R. S. 2002, ApJ, 573, 597
Li, J.-T., Bregman, J. N., Wang, Q. D., Crain, R. A., & Anderson, M. E. 2018, ApJL, 855, L24
Li, M., & Bryan, G. L. 2020, ApJL, 890, L30
Li, M., & Tonnesen, S. 2019, arXiv:1910.14235
Licquia, T. C., & Newman, J. A. 2015, ApJ, 806, 96
Lochhaas, C., Bryan, G. L., Li, Y., et al. 2020, MNRAS, 493, 1461
Maller, A. H., & Bullock, J. S. 2004, MNRAS, 355, 694
Manchester, R. N., Fan, G., Lyne, A. G., Kaspi, V. M., & Crawford, F. 2006, ApJ, 649, 235
Martin, C. L., Ho, S. H., Kacprzak, G. G., & Churchill, C. W. 2019, ApJ, 878, 84
Mathews, W. G., & Prochaska, J. X. 2017, ApJL, 846, L24
McConnachie, A. W., Venn, K. A., Irwin, M. J., Young, L. M., & Geehan, J. J. 2007, ApJL, 671, L33
McCourt, M., Sharma, P., Quataert, E., & Parrish, I. J. 2012, MNRAS, 419, 3319
McMillan, P. J. 2011, MNRAS, 414, 2446
McNamara, B. R., & Nulsen, P. E. J. 2007, ARA&A, 45, 117
McQuinn, M. 2014, ApJL, 780, L33
McQuinn, M., & Werk, J. K. 2018, ApJ, 852, 33
Meiring, J. D., Tripp, T. M., Werk, J. K., et al. 2013, ApJ, 767, 49
Miller, M. J., & Bregman, J. N. 2013, ApJ, 770, 118
Nelson, D., Genel, S., Pillepich, A., et al. 2016, MNRAS, 460, 2881
Nelson, D., Kauffmann, G., Pillepich, A., et al. 2018, MNRAS, 477, 450
Nicastro, F., Kaastra, J., Krongold, Y., et al. 2018, Natur, 558, 406
Ntormousi, E., & Sommer-Larsen, J. 2010, MNRAS, 409, 1049
Oppenheimer, B. D., Crain, R. A., Schaye, J., et al. 2016, MNRAS, 460, 2157
Oppenheimer, B. D., Segers, M., Schaye, J., Richings, A. J., & Crain, R. A. 2018, MNRAS, 474, 4740
Pedersen, K., Rasmussen, J., Sommer-Larsen, J., et al. 2006, NewA, 11, 465

Peek, J. E. G., Ménard, B., & Corrales, L. 2015, ApJ, 813, 7
Peeples, M. S., Corlies, L., Tumlinson, J., et al. 2019, ApJ, 873, 129
Peeples, M. S., Werk, J. K., Tumlinson, J., et al. 2014, ApJ, 786, 54
Pezzulli, G., Fraternali, F., & Binney, J. 2017, MNRAS, 467, 311
Planck Collaboration, Ade, P. A. R., Aghanim, N., et al. 2013, A&A, 557, A52
Planck Collaboration, Ade, P. A. R., Aghanim, N., et al. 2016, A&A, 594, A13
Prochaska, J. X., Macquart, J.-P., McQuinn, M., et al. 2019, Sci, 366, 231
Prochaska, J. X., & Tumlinson, J. 2009, ASSP, 10, 419
Prochaska, J. X., Weiner, B., Chen, H.-W., et al. 2011, ApJ, 740, 91
Prochaska, J. X., Werk, J. K., Worseck, G., et al. 2017, ApJ, 837, 169
Prochaska, J. X., & Zheng, Y. 2019, MNRAS, 485, 648
Putman, M. E., Peek, J. E. G., & Joung, M. R. 2012, ARA&A, 50, 491
Qu, Z., & Bregman, J. N. 2016, ApJ, 832, 189
Qu, Z., & Bregman, J. N. 2018a, ApJ, 856, 5
Qu, Z., & Bregman, J. N. 2018b, ApJ, 862, 23
Rasmussen, J., Sommer-Larsen, J., Pedersen, K., et al. 2009, ApJ, 697, 79
Ridley, J. P., Crawford, F., Lorimer, D. R., et al. 2013, MNRAS, 433, 138
Roca-Fàbrega, S., Dekel, A., Faerman, Y., et al. 2019, MNRAS, 484, 3625
Sadowski, A., & Gaspari, M. 2017, MNRAS, 468, 1398
Salem, M., Besla, G., Bryan, G., et al. 2015, ApJ, 815, 77
Salem, M., Bryan, G. L., & Corlies, L. 2016, MNRAS, 456, 582
Schaal, K., & Springel, V. 2015, MNRAS, 446, 3992
Sharma, P., McCourt, M., Parrish, I. J., et al. 2012a, MNRAS, 427, 1219
Sharma, P., McCourt, M., Quataert, E., et al. 2012b, MNRAS, 420, 3174
Singh, P., Nath, B. B., Majumdar, S., & Silk, J. 2015, MNRAS, 448, 2384
Smith, R. K., Abraham, M. H., Allured, R., et al. 2016, Proc. SPIE, 9905, 99054M
Spitzer, L., Jr. 1956, ApJ, 124, 20
Stern, J., Faucher-Giguère, C.-A., Hennawi, J. F., et al. 2018, ApJ, 865, 91
Stern, J., Fielding, D., Faucher-Giguère, C.-A., et al. 2019, MNRAS, 488, 2549
Stern, J., Fielding, D., Faucher-Giguère, C.-A., et al. 2020, MNRAS, 492, 6042
Sternberg, A., McKee, C. F., & Wolfire, M. G. 2002, ApJS, 143, 419
Strickland, D. K., Heckman, T. M., Colbert, E. J. M., Hoopes, C. G., & Weaver, K. A. 2004, ApJS, 151, 193
The LUVOIR Team 2018, arXiv:1809.09668
The Lynx Team 2018, arXiv:1809.09642
Tüllmann, R., Breitschwerdt, D., Rossa, J., Pietsch, W., & Dettmar, R.-J. 2006, A&A, 457, 779
Tumlinson, J., Peeples, M. S., & Werk, J. K. 2017, ARA&A, 55, 389
Tumlinson, J., Thom, C., Werk, J. K., et al. 2011a, Sci, 334, 948
Tumlinson, J., Werk, J. K., Thom, C., et al. 2011b, ApJ, 733, 111
Upton Sanderbeck, P. R., McQuinn, M., D'Aloisio, A., et al. 2018, ApJ, 869, 159
van Leeuwen, J., & Stappers, B. W. 2010, A&A, 509, A7
Voit, G. M. 2019, ApJ, 880, 139
Voit, G. M., Ma, C. P., Greene, J., et al. 2018, ApJ, 853, 78
Voit, G. M., Meece, G., Li, Y., et al. 2017, ApJ, 845, 80
Werk, J. K., Prochaska, J. X., Cantalupo, S., et al. 2016, ApJ, 833, 54
Werk, J. K., Prochaska, J. X., Thom, C., et al. 2013, ApJS, 204, 17
Werk, J. K., Prochaska, J. X., Tumlinson, J., et al. 2014, ApJ, 792, 8
White, S. D. M. 1978, MNRAS, 184, 185
Wolfire, M. G., McKee, C. F., Hollenbach, D., & Tielens, A. G. G. M. 2003, ApJ, 587, 278
Zheng, Y., Peek, J. E. G., Putman, M. E., & Werk, J. K. 2019, ApJ, 871, 35
Zheng, Y., Putman, M. E., Peek, J. E. G., & Joung, M. R. 2015, ApJ, 807, 103